A circuit involving the lncRNA MB3 and the driver genes MYC and OTX2 inhibits apoptosis in Group 3 Medulloblastoma by regulating the TGF-β pathway via HMGN5

Grandioso Alessia[1], Tollis Paolo[2], Pellegrini Francesca Romana[3], Falvo Elisabetta[3], Palma Alessandro[1], Migliaccio Francesco[4], Belvedere Alessandro[1], Rea Jessica[2], Tisci Giada[1,5], Carissimo Annamaria[6], Bozzoni Irene[1,2], Trisciuoglio Daniela[3], Ballarino Monica[1], Ceci Pierpaolo[3], Laneve Pietro[1,3,#]

1. Department of Biology and Biotechnologies Charles Darwin, Sapienza University of Rome, Piazzale Aldo Moro 5, 00185, Rome, Italy.
2. Center for Life Nano-& Neuro-Science, Fondazione Istituto Italiano di Tecnologia, Viale Regina Elena 291, 00161, Rome, Italy.
3. Institute of Molecular Biology and Pathologies, National Research Council of Italy, Piazzale Aldo Moro 7, 00185, Rome, Italy.
4. Department of Electrical Engineering and Information Technology, University Federico II, Via Claudio 21, 80125, Naples, Italy.
5. Department of Biochemical Sciences, Sapienza University of Rome, Piazzale Aldo Moro 5, 00185, Rome, Italy.
6. Institute for Applied Mathematics "Mauro Picone", National Research Council of Italy, Via Pietro Castellino 111, 80131 Naples, Italy.

correspondence to: Pietro Laneve, IBPM-CNR, c/o Sapienza University of Rome, Piazzale Aldo Moro 5, 00185, Rome, Italy. E-mail: pietro.laneve@cnr.it; Phone: +390649912205

Running title: *LncMB3* controls TGF-β pathway in Medulloblastoma

ABSTRACT

Background. Group 3 (G3) is one of the most common, aggressive and fatal subtypes of the paediatric cerebellar tumour Medulloblastoma (MB), primarily driven by the MYC oncogene. Targeting MYC has long been challenging and this, combined with our incomplete understanding of G3 MB molecular bases, has hindered the development of effective targeted therapies. Long noncoding RNAs (lncRNAs), with their extensive oncogenic roles, cancer-specific expression, and connection to MYC biology, offer opportunities for unravelling this complexity and providing new insights and therapeutic targets.
Methodology. Using genome-wide, molecular and cellular assays, we characterised the activity of the MYC-dependent, anti-apoptotic lncRNA *lncMB3* in G3 MB cells.
Results. Through transcriptomic and interactomic analyses, we clarified *lncMB3* function and mode-of-action. *LncMB3* controls the TGF-β pathway, critically altered in G3 medulloblastomagenesis. This regulation occurs via the direct coding-noncoding RNA interaction between *lncMB3* and the mRNA for the epigenetic factor HMGN5, with both sharing targets in the TGF- β cascade. This axis converges on apoptosis through OTX2, another G3 MB driver gene, and photoreceptor lineage genes. Synergistic effects between *lncMB3* targeting and cisplatin treatment underscores the relevance of this regulatory network *in vitro*. Finally, we propose novel ferritin-based nanocarriers as efficient delivery tools for antisense oligonucleotides targeting *lncMB3*.
Conclusions. *LncMB3* emerges as a central node linking MYC amplification to apoptosis inhibition through a circuit involving RNA-based mechanisms, G3 MB key drivers and underexplored factors.

47 This integrated framework deepens our understanding of G3 MB molecular underpinnings and lay
48 the foundation for translating lncRNA research into potential applications.
49

50 **INTRODUCTION**

51 Medulloblastoma (MB) is the most prevalent malignant paediatric tumour in the central nervous
52 system, accounting for ~20% of all brain cancers in children [1], [2]. Although all MBs originate in the
53 cerebellum, share histomorphological features, and possess signatures of embryonic cerebellar
54 lineages [3], they exhibit high heterogeneity. MB is classified into 4 subtypes with distinct biological,
55 clinical and therapeutical implications [4]: Wingless (WNT), Sonic Hedgehog (SHH), Group 3 (G3) and
56 Group 4 (G4). G3 and G4, collectively, account for 60% of MB cases and represent the most
57 aggressive subtypes, posing significant treatment challenges due to their poor biochemical
58 characterisation. Understanding the molecular mechanisms behind these subgroups is critical for
59 advancing precision medicine strategies. Specifically, G3 MB is associated with a dismal prognosis,
60 often presenting with metastases at diagnosis and exhibiting high recurrence rates [2]. It is driven
61 primarily by the oncogenic transcription factor (TF) MYC, whose gene copy number amplification or
62 elevated expression are distinctive of this subtype [5]. Targeting MYC and its related
63 pathways/complexes is essential for managing G3 MB, despite the challenges associated with
64 addressing canonical MYC circuits [6].

65 The discovery of novel classes of noncoding RNAs (ncRNAs) is expanding our understanding of
66 genome output and function [7], offering new avenues for cancer therapeutics. Among ncRNAs, the
67 highly versatile long noncoding RNAs (lncRNAs) have emerged as key regulators of cancer hallmarks
68 [8], showing potential as biomarkers and targets due to their cell-specific expression and regulatory
69 activities. Over the years, we have unravelled the roles of ncRNAs in various nervous system cancer
70 models, including MB [9]. Recently, we identified in G3 MB a class of MYC-dependent lncRNAs, with
71 three of them showing a potential function as oncogenes [10], including *lncMB3*.

72 In this study, we present a detailed functional analysis of *lncMB3*, which is overexpressed in the
73 tumour condition and acts as anti-apoptotic factor. We show that *lncMB3* regulates the TGF-β
74 pathway, a key player known to be altered in G3 MB [11]. This is achieved by a functional interaction
75 with the mRNA of the epigenetic factor HMGN5, whose protein level is upregulated and impacts on
76 a subset of TGF-β pathway genes also affected by *lncMB3* targeting. Notably, coding-noncoding RNA
77 interplays are increasingly recognised as important mechanisms in cancer biology. This regulatory
78 axis influences apoptosis through OTX2, an additional crucial G3 MB driver gene [12], and its
79 downstream cascade. The relevance of this circuit is underscored by the synergistic effects observed
80 when *lncMB3* targeting is combined with cisplatin administration in G3 MB cells. Lastly, we
81 demonstrate that recombinant human ferritin-based nanovectors, a promising platform for drug
82 administration in disease conditions [13], serve as effective carriers for delivering antisense
83 oligonucleotides (ASOs) targeting *lncMB3* in G3 MB cells.
84
85 **RESULTS**
86 **Identification of *lncMB3*-dependent transcriptome in G3 MB cells**
87 To identify the molecular network downstream of *lncMB3* in MB, we performed a transcriptome
88 analysis following its knockdown (KD) in the MYC-amplified D283 Med cell line where the lncRNA is
89 highly expressed (Fig. S1A) and initially identified [10]. According to GTEx
90 (https://gtexportal.org/home/), *lncMB3* is minimally expressed in healthy tissues (Fig. S1B). The KD
91 of *lncMB3* reduced its expression by ~70% (Fig. S2A) 72 hours after multi-pulse transfections of a
92 Locked Nucleic Acid (LNA)-based ASO [14], named GapmeR #1, which targets the lncRNA at its 5'
93 region. Initial transcriptional data analysis yielded positive results regarding the number of detected
94 genes (Fig. S2B, left panel), clustering of transcriptomes (Fig. S2B, right panels) and consistency
95 between *lncMB3* KD normalised read counts and previous qRT-PCR assessments (Dataset 1).

96 RNA-Seq analysis (Dataset 1) identified 14.655 transcripts expressed in at least one sample, and
97 2.995 differentially expressed genes (DEGs) between *lncMB3* KD and control (SCR), with an FDR <
98 0,05 (Fig. 1A, left panel). Among these, 1.395 were downregulated and 1.600 were upregulated
99 following *lncMB3* silencing (Fig. 1A, right panel, blue and red dots). A dozen of these upregulated or
100 downregulated genes were randomly selected, with padj ranging from 0,001 to 0,05, for qRT-PCR
101 validation, which confirmed RNA-Seq expression data (Fig. S2C and Dataset 1).
102 To functionally explore the transcriptomic landscape, DEGs were filtered using quantitative criteria,
103 such as fold change (FC) robustness, statistical significance, and expression levels (Fig. S2D). We
104 identified 13 RNAs regulated by *lncMB3* (12 protein-coding transcripts and 1 lncRNA, being 7
105 significantly downregulated and 6 upregulated RNAs, Dataset 2). qRT-PCR validated RNA-Seq data
106 trends for the selected DEGs, demonstrating statistical significance (for 10 out of 13 genes) or, at
107 least, discernible variance trends (Fig. S3A). Notably, the top gene identified was *INHBE*, a
108 component of the TGF-β pathway [15], associated with G3 MB pathogenesis [11].
109 Gene Ontology (GO) analysis was performed on DEGs to identify the full set of gene functions
110 affected by *lncMB3* depletion (Fig. 1B, left panel). Concerning the ontological annotations, among
111 the top categories, GO revealed pathways such as "PIK3-Akt signalling" known to affect
112 chemosensitivity in various cancers, including MB [16], and "MAPK signalling" possibly reflecting
113 DNA damage response to apoptosis induced by *lncMB3* KD. Our focus, however, was again on the
114 TGF-β pathway, which emerged as the second top gene category and is deregulated in G3 MB
115 compared to other subgroups. Moreover, the TGF-β pathway was a category present in both the up
116 and downregulated gene sets (Fig. S3B), suggesting deregulation of activatory and inhibitory
117 effectors in the same pathway. Finally, Gene Set Enrichment Analysis (GSEA) further confirmed the
118 TGF-β pathway as significantly affected by *lncMB3* KD in G3 MB cells (Fig. S3C).
119

120 ***LncMB3* regulates the TGF-β pathway in G3 MB**

121 Aberrant TGF-β signalling plays a key role in the development of various diseases, including cancer
122 [17]. In G3 MB, its deregulation is believed to drive processes such as cell proliferation,
123 differentiation, and survival [11].

124 The importance of this pathway in our system was further highlighted by filling the category with
125 additional DEGs involved in the pathway. We finally identified a set of 9 genes, including TGF-
126 β/Activin signalling ligands (*INHBE*, [15]; *THBS1*, *THBS3*, [18]), receptors (*ACVR1B*,[19]; *BAMBI*, [20]),
127 effectors (*SMAD3*, *SMAD6*, *SMAD7*, [19]), and downstream regulators (*TFDP1*, [21]) (Fig. S3D). qRT-
128 PCR upon *lncMB3* KD revealed the repression of genes with activatory roles in the pathway (*THBS1*,
129 *THBS3*, *INHBE*, *ACVR1B*, *SMAD3*, *SMAD6*, *SMAD7*), with downregulations ranging from 20% to 80%
130 (Fig. 1B, right panel). Conversely, inhibitory components (*BAMBI* and *TFDP1*) were upregulated
131 under the same conditions (1.5- to 3-fold, Fig. 1B, right panel), suggesting a coherent contribution
132 of both positive and negative regulators that leads to an overall downregulation of the TGF-β/Activin
133 branch. To ensure specificity in targeting, we employed an additional GapmeR (GapmeR #2), which
134 recognises the 3' end of *lncMB3* (Fig. S4A). This achieved a 70% depletion of the transcript in D283
135 Med cells (Fig. S4B). To further corroborate these findings, we also used GapmeR #2 to target *lncMB3*
136 in HD-MB03, a G3 MB cell line where MYC and *lncMB3* are upregulated (Fig. S1A). This led to a 50%
137 reduction of the lncRNA levels (Fig. S4B). Validation data showed similar expression alterations in all
138 the condition tested for 5 TGF-β network genes: *BAMBI*, *ACVR1B*, *INHBE*, *SMAD3*, and *SMAD6* (Fig.
139 1C). Since GapmeR #1 targets the 5' end of *lncMB3* and results in a more efficient downregulation
140 (Fig. S4B), it was preferentially used in subsequent experiments. Overall, the RNA-Seq analysis clearly
141 points to a regulatory role of *lncMB3* in the TGF-β pathway in G3 MB cells.

142

143 **Insights into apoptosis regulation by *lncMB3***

144 In the developing nervous system, a relevant target of the TGF-β cascade is the brain-specific TF
145 OTX2, recognised as a G3 MB-enriched oncogene [12] and upregulated in both D283 Med and HD-
146 MB03 cells (Fig. S1A). During retinal development, OTX2 occupies a pivotal position in a hierarchy of
147 photoreceptor lineage genes, including the basic leucine zipper TFs *NRL* and *CRX* [22]. These factors
148 are overexpressed in G3 MB, where they mediate cancer survival by inducing the expression of the
149 anti-apoptotic factor *BCL2L1* ([23] and Fig. S3D).
150 We queried an available transcriptomic dataset (GSE164677) from 59 patient-derived samples
151 representing all MB subgroups and 4 control samples to evaluate the expression of these genes in
152 primary MB tumours. The expression of *NRL*, *CRX*, and *BCL2L1* was significantly upregulated in G3
153 compared to either healthy tissues or other MB subgroups. Although the upregulation of *OTX2* in
154 G3 MB compared to cerebellum samples did not reach statistical significance, it exhibited an upward
155 trend (Fig. 2A). Figure 2B (left panel) outlines the connections among these factors. Consistent with
156 this model, photoreceptor gene program was categorised in several downregulated annotations in
157 *lncMB3* KD-dependent GSEA (Fig. 2B, middle panel).
158 Given this context, we observed the downregulation of *OTX2*, *NRL*, *CRX*, and *BCL2L1* RNAs in D283
159 Med cells following *lncMB3* depletion (Fig. 2B, right panel). Protein downregulation was also
160 assessed for OTX2 and BCL2L1 (Fig. 2C), as well as for PARP-1 (Fig. 2D) [24], whose cleavage (C-PARP)
161 is a hallmark of apoptosis. The involvement of the lncRNA in this axis was further confirmed using
162 GapmeR #1 in HD-MB03 cells, where *lncMB3* depletion led to i) decreased RNA and protein levels
163 for OTX2, NRL, CRX, and BCL2L1 (Fig. 3A and B); ii) reduced cell viability (Fig. 3C); and iii) coherent
164 modulation of C-PARP and PARP-1 levels (Fig. 3D).
165 Consistent with *lncMB3* being regulated by MYC [10], the *lncMB3*-dependent RNA alterations
166 highlighted here were also observed in the transcriptome of MYC-inhibited D283 Med cells *vs*
167 untreated cells (Dataset 3). To further demonstrate that *lncMB3* and the TGF-β pathway are part of

168 the same regulatory network, we utilised a TGF-β Receptor 1 Kinase inhibitor, which prevents
169 Smad2/3 phosphorylation. After 48 hours of treatment, we observed a dose-dependent reduction
170 in the number of viable cells (Fig. 3E). This cell phenotype was correlated with increased apoptosis,
171 as confirmed through the Annexin V binding assay (Fig. 3F). This shows that direct inhibition of the
172 TGF-β cascade leads to effects converging with those observed upon *lncMB3* silencing.
173 To definitively establish the function of *lncMB3* in counteracting apoptosis, we performed a rescue
174 assay in G3 MB. We generated a plasmid carrying the lncRNA sequence lacking the first 16
175 nucleotides (Δ16), which are necessary for recognition by GapmeR #1 (Fig. 3G, left panel). When
176 overexpressed in D283 Med cells along with the ASO, this construct successfully expressed a mutant
177 lncRNA derivative (Fig. 3G, middle panel), and restored cell viability compared to cells transfected
178 with GapmeR #1 alone (Fig. 3G, right panel).
179 These findings allow us to reconstruct a molecular network initiated by MYC amplification and
180 involving a non-coding RNA, which leads to the suppression of apoptosis in G3 MB.
181
182 **Insights into the RNA interactome of *lncMB3***
183 RNA-RNA pairing is a crucial mechanism for lncRNA functionality. Given this and *lncMB3*
184 nucleocytoplasmic localisation in MB cells, we investigated whether the lncRNA could modulate the
185 expression of TGF-β and apoptotic pathway genes through such interactions.
186 Initially, we hypothesized a straightforward interaction between *lncMB3* and candidate mRNAs
187 downregulated upon its KD. However, preliminary analyses using the IntaRNA algorithm
188 (http://rna.informatik.uni-freiburg.de/), which maps transcript binding regions, yielded low
189 interaction propensity (Table 1). To experimentally explore possible indirect associations, we
190 performed RNA pull-down assays as in [25] (Fig. 4A). qRT-PCR analysis comparing *lncMB3*-enriched
191 pull-down fractions with EVEN and ODD probe sets with mock-precipitated LacZ fractions (Table 2)

192 showed no significant enrichment for any tested candidate (Table 3), excluding molecular
193 interactions between *lncMB3* and transcripts of the TGF-β and downstream pathways.
194 We then focused on the competing endogenous RNA network, where long RNAs modulate
195 microRNA activity by sponging them [26]. Preliminary interactions between *lncMB3* and the core
196 RNA-induced silencing complex component Argonaute 2 (AGO2) were predicted via the *cat*RAPID
197 algorithm (http://s.tartaglialab.com/page/catrapid_group) (Dataset 4) and experimentally validated
198 through a CLIP assay (Fig. S5A). Based on these results, we employed Targetscan
199 (https://www.targetscan.org/vert_80/) to identify microRNAs predicted to bind both *lncMB3* and
200 candidate mRNAs (Table 4). Among the six candidates (*hsa-miR-135b-5p*, *hsa-miR-216a-3p*, *hsa-miR-*
201 *3681-3p*, *hsa-miR-613*, *hsa-miR-1197*, *hsa-miR-196b-5p*), the top three were tested by qRT-PCR on
202 *lncMB3* pull-down fractions, but none of them showed significant enrichment, ruling out
203 competition for microRNA association in the context investigated (Table 5).
204 An alternative scenario suggests that *lncMB3* could regulate its target genes via interactions with
205 other mRNAs [27]. To explore this, we identified *lncMB3* interactome crossing RNA-Seq data from
206 replicate independent *lncMB3* pull-down experiments (Fig. 4B and Dataset 5) and performing a
207 stringent analysis to highlight the predominant binding partners. We found two mRNAs (*HMGN5*,
208 *EIF5B*) and one lncRNA (*ANKDDA1*) associated to *lncMB3* (Fig. 4B and Fig. S6A), with the mRNA for
209 the nuclear factor HMGN5 (High Mobility Group Nucleosome Binding Domain 5) showing the highest
210 FC and the most significant FDR. Given the broad epigenetic role of HMGN5 in transcriptional
211 regulation [28], its interplay with *lncMB3* underlined this factor as a candidate for further analysis.
212
213 ***LncMB3* interacts with *HMGN5* mRNA**
214 The chromatin factor HMGN5 regulates gene expression by modulating interactions between
215 nucleosomes and DNA [28], [29]. *HMGN5* is expressed ubiquitously (Fig. S6B), and, among brain

216 tissues, its expression is low in cerebellum. Interestingly, RNA-Seq data from the primary MB dataset
217 GSE164677 revealed *HMGN5* upregulation, with a more pronounced tendency in G3 (Fig. 4C).
218 Co-enrichment of *HMGN5* mRNA with *lncMB3* was validated in an additional pull-down assay (Fig.
219 4D). IntaRNA predicted an interaction site (energy score: -30,1 kcal/mol) spanning ~120 nucleotides
220 over the 5' region of *lncMB3* (nt 189-307) and the coding sequence of *HMGN5* mRNA (nt 933-1059)
221 (Fig. 4E). This prediction was experimentally verified using a 4'-aminomethyl-4,5',8-
222 trimethylpsoralen (AMT)-crosslinked RNA pull-down assay [25], which highlights direct RNA-RNA
223 pairings *in vivo* (Fig. 4F). Interestingly, digital PCR-based absolute quantifications of *lncMB3* and
224 *HMGN5* abundance showed that their expression levels were stoichiometrically equivalent (Fig.
225 S6C).
226 To assess the functional consequences of this interaction, we investigated whether *lncMB3* affects
227 *HMGN5* expression. *HMGN5* mRNA levels were unchanged by *lncMB3* KD, as indicated by RNA-Seq
228 data (Dataset 1) and confirmed by qRT-PCR (Fig. S7A). However, HMGN5 protein levels decreased by
229 ~80% upon *lncMB3* KD (Fig. 4G), consistently with the oncogenic activity attributed to HMGN5 in a
230 spectrum of cancers [30], [31]. Rescue of *lncMB3* levels through transient exogenous expression of
231 Δ16 construct (Fig. 3G, left panel) showed a recovery trend for HMGN5 levels (Fig. 4G), indicating
232 that HMGN5 protein levels are regulated by *lncMB3* in a specific, quantitative manner.
233 The impact of *lncMB3* on HMGN5 protein levels, along with their RNA interaction, indicates a role
234 for the lncRNA as a translational activator. This was confirmed using a Ribo-Tag strategy [32] with
235 transient expression of a FLAG-tagged version of the 60S ribosomal protein L22 (RPL22) in D283 Med
236 cells (Fig. S7B). Western blot analysis of FLAG-RPL22-precipitated fractions showed comparable
237 levels of FLAG-RPL22 in gap_SCR *vs* gap_*lncMB3* protein extracts (Fig. S7C). At variance, qRT-PCR
238 analysis showed a consistent decrease of *HMGN5* mRNA association to ribosomes in the absence of

239 *lncMB3*, compared to *GAPDH* as a control (Fig. 4H). These results indicate that *lncMB3* is required
240 for *HMGN5* mRNA association with ribosomes.
241
242 **HMGN5 regulates the TGF-β pathway and apoptosis in G3 MB cells**
243 Given HMGN5 documented activity in the nucleus, we re-examined the expression of genes altered
244 by *lncMB3* KD to assess whether their up or downregulation was primarily due to transcriptional
245 regulation. qRT-PCR analysis was performed using exonic primers *vs* primers spanning exon-intron
246 junctions, to distinguish mature mRNAs from primary transcripts. As shown in Fig. S7D, *lncMB3*
247 silencing led to the downregulation of *ACVR1B*, *INHBE*, *SMAD3*, *OTX2*, *NRL*, and *CRX* pre-mRNAs,
248 highlighting a nuclear control over several genes regulated by *lncMB3* (compare Figs 1B, 1C, 2B, 3A).
249 A role for HMGN5 in suppressing apoptosis had not previously been assessed in MB. To establish a
250 functional connection between *lncMB3* and HMGN5 activities, we sought to mimic the molecular
251 effects of *lncMB3* KD by silencing *HMGN5*. We designed a short interfering RNA targeting *HMGN5*
252 with VectorBuilder (https://en.vectorbuilder.com/). Transient transfection of this construct in D283
253 Med cells resulted in a ~30% downregulation of *HMGN5* mRNA (Fig. 4I) and a ~60% reduction in
254 protein levels (Fig. S7E). This led to a 20-50% RNA decrease for *INHBE*, *SMAD3*, *OTX2*, and *BCL2L1*
255 (Fig. 4I), which are among the targets identified upon *lncMB3* KD (see Figs 1B, 1C, 2B, 3A). This
256 indicates that the achieved levels of *HMGN5* KD appreciably phenocopy the molecular effects of
257 *lncMB3* downregulation (Fig. S7F). Regarding cell death, after *HMGN5* KD we also observed a
258 threefold increase in c-PARP1 protein (Fig. 4J, left panel) and a 30% decrease in full-length PARP1
259 (Fig. 4J, right panel). Reduction in HMGN5 levels also phenocopied the decrease in the number of
260 viable D283 Med cells, with a drop of ~30% (Fig. 4K), similarly with the effects of *lncMB3* targeting.
261 Overall, these findings indicate that *lncMB3* and HMGN5 functionally participate into the same
262 molecular and cellular phenotypes. Interacting with *lncMB3*, *HMGN5* mRNA decreased translation

263 contributes to the nuclear regulation of the TGF-β pathway and of the downstream gene module in
264 G3 MB cells.
265
266 ***LncMB3* inhibition synergizes with DDP treatment in G3 MB cells**
267 Cisplatin (DDP) is a first-line anti-cancer agent and a cornerstone of MB treatment [33]. Combining
268 therapies has been shown to reduce DDP side effects and overcome both intrinsic and acquired
269 cancer resistance. Based on the shared influence of *lncMB3* and DDP on apoptosis-related signalling
270 pathways [34], we explored whether *lncMB3* KD could enhance DDP cytotoxicity in G3 MB cells.
271 Initial tests of DDP administration to D283 Med cells at concentrations of 1-10µM reduced the
272 number of viable cells by 10%-20% after 48 hours (Fig. 5A, left panel). We then combined 10µM DDP
273 with transfection of 100nM GapmeR #1 or GapmeR #2 and counted the surviving cells.
274 Normalisation of cell counts from double-treated *vs* drug-untreated samples showed a reduced
275 relative cell survival rate in gap_*lncMB3*-treated cells compared to scramble-transfected controls,
276 indicating a synergistic effect between GapmeR and DDP treatments (Fig. 5A, right panel). This was
277 further confirmed through an apoptotic assay based on Annexin V staining (Fig. 5B, left panel).
278 Quantification of non-viable *vs* viable cells showed that combined treatments caused an increase of
279 late apoptotic cell number compared to other cell populations (Fig. 5B, middle panel), confirming a
280 synergistic effect (Fig. 5B, right panel).
281 We also examined whether this synergistic activity could be explained by crosstalk between the two
282 treatments. Testing the effect of DDP on the genes of interest revealed that cisplatin partially
283 deregulates both the TGF-β (Fig. 5C, left panel) and apoptotic pathway (Fig. 5C, right panel), similarly
284 to *lncMB3* targeting. Notably, *lncMB3* expression was not affected by chemotherapy (Fig. S8A),
285 suggesting that the two treatments represent independent triggers with overlapping outcomes.

286 It is worth noting that the synergistic enhancement of anticancer effects achieved through *lncMB3*
287 targeting was not indiscriminate. When we tested the concurrent use of GapmeR #1 and vincristine,
288 another drug used in MB therapy [35], we observed only additive, not synergistic effects on viable
289 cell counts (Fig. S8B) and apoptosis (Fig. S8C). These data suggest that *in vitro*, *lncMB3* targeting
290 synergistically enhances the efficacy of DDP treatment in reducing G3 MB cell proliferation and
291 inducing apoptosis.
292
293 **Production of the ferritin variant HFt-HIS-PASE**
294 Targeting *lncMB3* impacts the TGF-β pathway, enhances apoptosis, and improves chemotherapeutic
295 efficiency in cancer cell lines. These findings encouraged us to explore the use of recombinant
296 human ferritin nanoparticles (NPs) to formulate innovative RNA/protein complexes for *lncMB3*-
297 directed GapmeR delivery. Human ferritin H-type (HFt) is a promising NP for drug delivery, especially
298 chemotherapeutics, due to its ability to be internalised by the transferrin receptor 1 (TfR1 or CD71),
299 often overexpressed in tumour cells [13].
300 We designed and synthesized HFt-HIS-PASE, a recombinant ferritin variant derived from a previously
301 described version of HFt, i.e. HFt-MP-PASE [36]. HFt-HIS-PASE contains a tumour-selective sequence
302 (MP) responsive to proteolytic cleavage by specific tumour proteases (MMP 2 and 9), and a shielding
303 polypeptide (PASE) that increases stability, masks the surface, and improves target specificity.
304 Additionally, HFt-HIS-PASE includes a five-histidine motif reported to enhance endosomal escape of
305 nucleic acids [37] (Fig. S9A).
306 Preliminary assessments of *MMP 2*, *MMP 9*, and *CD71* mRNA abundance in D283 Med and HD-MB03
307 cells via qRT-PCR (Fig. S9B) led to the selection of D283 Med cells for further experiments. We then
308 evaluated the targeting capability of a Fluorescein-5-Maleimide-labeled HFt-HIS-PASE nanovector
309 (HFt-HIS-PASE-fluo). D283 Med cells were cultured with HFt-HIS-PASE-fluo (1mg/mL) and 12 hours

310 post-administration ~85% of cells exhibited green fluorescence, confirming their affinity for HFt-HIS-
311 PASE (Fig. 6A). Immunofluorescence performed on these samples 24 hours later, with nuclear (DAPI)
312 and cytoplasmic (Phalloidin) staining, and confocal laser microscopy analysis, revealed intracellular
313 uptake of HFt, with a nuclear-cytoplasmic distribution (Fig. 6B).
314
315 **Characterisation of HFt-HIS-PASE-GapmeR complexes and *lncMB3* targeting**
316 To investigate the potential of targeting *lncMB3* using HFt-ASO complexes, we generated and
317 characterised HFt-HIS-PASE-GapmeR nucleoprotein particles. The *lncMB3* GapmeR #1 was
318 encapsulated within the internal cavity of HFt-HIS-PASE using a pH-dependent
319 dissociation/reassociation strategy. Successful loading of the GapmeR payload was verified via
320 electrophoresis of the purified HFt-HIS-PASE-GapmeR complexes. Distinct migration patterns were
321 observed for the HFt-HIS-PASE-GapmeR complex compared to the free GapmeR. When visualised by
322 DNA-specific staining (Fig. 6C, left panel), the nucleic acid displayed a significant delay when
323 associated with HFt-HIS-PASE (lane HFt + gap), compared to the free GapmeR. Protein-specific
324 staining showed that the HFt-HIS-PASE-GapmeR complex co-migrated with ferritin (Fig. 6C, right
325 panel).
326 Concerning complex stability, no evidence of nucleic acid degradation was observed after 1 hour and
327 overnight incubations of HFt-HIS-PASE-GapmeR with DNA/RNA nuclease (Denarase) at 37°C (Fig.
328 S9C). Additionally, no degradation was observed after 3 months of storage at 4°C (data not shown),
329 confirming that GapmeR was encapsulated and protected within the protein cavity and not exposed
330 to external surface.
331 To evaluate the efficiency of GapmeR binding to HFt NPs, the relative intensities of agarose bands
332 corresponding to DNA or protein molecules were quantified. Comparisons were made to free
333 GapmeR and HFt-HIS-PASE molecules in standard concentration as references. The final GapmeR-

334 HFt-HIS-PASE molecular ratio was determined to be 0,5:1. Purity and hydrodynamic volume of the
335 HFt-HIS-PASE-GapmeR complexes were assessed via size-exclusion chromatography. The HFt-HIS-
336 PASE-GapmeR sample displayed an elution volume and size similar to non-encapsulated HFt-HIS-
337 PASE protein, with no free GapmeR observed, indicating that GapmeR molecules in solution co-
338 eluted with ferritin (Fig. 6D).
339 The biological activity of the complex was tested in D283 Med cells treated with a single dose of HFt-
340 HIS-PASE alone or HFt-HIS-PASE-GapmeR complex (200nM). Steady-state *lncMB3* expression levels,
341 assessed 48 hours after administration, showed a 30% reduction following encapsulated GapmeR #1
342 delivery compared to mock-treated cells (Fig. 6E). Similar results were obtained after re-testing HFt-
343 HIS-PASE-GapmeR samples stored at 4°C for 3 months. This setup simulated the effects of a standard
344 single-pulse transfection of GapmeR #1 at 100nM for 48 hours (Fig. S9D). Likely due to insufficient
345 *lncMB3* downregulation, we observed no modulation of TGF-β pathway genes, no reduction in cell
346 proliferation, nor any increase in apoptosis under these conditions.
347 However, to further explore the cellular effects of HFt-HIS-PASE-mediated *lncMB3* targeting, we
348 leveraged our earlier findings on the synergistic interplay between *lncMB3* KD and DDP treatment.
349 D283 Med cells were treated with 5µM DDP alone or in combination with HFt-HIS-PASE-GapmeR. In
350 the latter condition, we observed by qRT-PCR that combined DDP and GapmeR #1 administration
351 led to reduction in TGF-β pathway and downstream genes, ranging from 20% to 50% (Fig. 6F).
352 Consistent with previous observations (Fig. 5A), there was also a decrease in cancer cell survival
353 following the combined treatments, compared to DDP treatment alone (Fig. 6G). These results
354 confirm the efficacy of *lncMB3* targeting, facilitated by an HFt-based delivery system, in sensitising
355 G3 MB cells to anticancer drugs.
356
357 **DISCUSSION**

358 Integrated multi-omics has enabled the combination of genetic and histological analyses within a
359 framework for understanding the inherent heterogeneity and complexity of MB [1]. Despite unique
360 genomic, biochemical and clinical traits of each MB subgroup [38], current therapeutic strategies
361 still rely on general interventions, including surgical resection, chemotherapy, and radiotherapy,
362 with 5-year survival rates ranging from 60% to 80% [39]. This underscores the need for targeted
363 therapies and deep explorations of dysfunctional pathways, particularly in high-risk and poorly
364 characterised subgroups, such as G3 and G4. G3 MB, which accounts for 25% of cases, exhibits the
365 highest recurrence rate and a strong propensity for metastasis, correlating with significantly worse
366 outcomes [40]. The discovery of MYC amplification/overexpression as a major pathogenic factor
367 [41], [42] is consistent with estimates of aberrant MYC activity in nearly 70% of human cancers [42].
368 However, targeting MYC has long been challenging due to its disordered structure, which has led to
369 candidate therapeutic molecules with low potency, suboptimal pharmacological properties, and
370 considerable off-target effects [43]. Furthermore, MYC plays a critical role in physiological
371 processes, including cell differentiation, proliferation, and cell cycle regulation, which are central to
372 development and post-natal life. This makes it essential to develop strategies for MYC inhibition
373 particularly in paediatric cancers. Several pre-clinical studies and clinical trials are currently
374 exploring direct MYC inhibitors [43], [44], such as the dominant-negative OMOMYC, that showed
375 promising results in solid cancers [10], [44] and that we used to map the MYC transcriptome in G3
376 MB cells [10]. Indirect strategies that target MYC cofactors or regulators represent a viable
377 alternative for functional MYC inhibition. Along this direction, a comprehensive understanding of
378 MYC-dysregulated gene pathways, including non-coding RNA networks, may diversify and enhance
379 opportunities for MYC-targeted therapies [45].
380 Over the past two decades, the rise of non-coding RNAs has revolutionised cancer biology [46].
381 LncRNAs have gained attention as modulators of cancer hallmarks due to their tissue- and cell-type-

382 specific expression and structural flexibility, making them attractive biomarkers and targets for
383 molecular medicine. However, their potential as master regulators of biological processes require
384 comprehensive functional characterisation.
385 To date, only 3 lncRNAs have been mechanistically described in G3 MB. This study elucidates the
386 role of the MYC-regulated *lncMB3* in G3 medulloblastomagenesis and lays the foundation for its
387 potential applicative use. *LncMB3* is upregulated in G3 MB cell lines and primary tumours and
388 exhibits a strong activity in evading cell death *in vitro*. Through transcriptomic, molecular, and
389 cellular assays, we demonstrate that *lncMB3* plays a crucial role in controlling the TGF-β cascade, a
390 key player in G3 MB pathology, influencing cancer cell proliferation and survival [11]. Notably, we
391 identified a cluster of *lncMB3* target genes in this pathway, whose aberrant expression leads to
392 overexpression of the retinal TF OTX2, an oncogenic event in G3 MB that promotes cell proliferation,
393 inhibits apoptosis, and contributes to tumour aggressiveness [47]. OTX2 and other photoreceptor
394 TFs, including NRL and CRX, drive the expression of anti-apoptotic factors like BCL2L1 [23], linking
395 this gene program to the sustained viability of cancer cells. *LncMB3* regulatory activity orchestrates
396 critical pathways, genes, and processes in G3 MB, forming a nexus among the *MYC* driver gene, the
397 TGF-β signalling, photoreceptor gene network, and apoptosis regulators. This interconnection offers
398 an integrated framework for understanding the molecular underpinnings of this tumour subgroup.
399 While our coding transcriptome analysis provided insights into *lncMB3* function, the exploration of
400 its interactome revealed its mode of action. *LncMB3* directly interacts with the mRNA encoding the
401 epigenetic regulator HMGN5, a member of the HMGN nucleosome-binding and nuclear architecture
402 family that extensively regulates chromatin decondensation and transcription [30], [31]. *HMGN5*,
403 which plays a role in embryonic gene regulation [48] and displays oncogenic properties in several
404 cancers [30], [31], is upregulated in G3 MB. Our findings suggest that RNA-RNA interactions between
405 coding and non-coding molecules, an emerging theme in cancer regulation, result in the functional

406 upregulation of HMGN5 protein levels, explaining why *HMGN5* RNA interference phenocopies the
407 effects of *lncMB3* targeting. Since several *lncMB3* targets are dysregulated in the nucleus, where
408 HMGN5 operates, the mechanism we propose adequately accounts for the observed molecular and
409 cellular phenotypes. This does not exclude the possibility of additional regulative cascades or
410 secondary effects, which could align with the recently suggested moonlighting role for HMGN5 in
411 RNA binding [48]. Finally, *lncMB3* and *HMGN5* co-expression, confined to pathological cerebellum,
412 proposes their interaction as a platform for developing innovative inhibitors to compete with
413 disease-specific complexes.
414 Due to the aggressive nature of G3 MB and its resistance to treatments, integrated therapies offer
415 promising solutions. Meanwhile, ASOs have gained prominence in RNA-based treatments due to
416 their flexible design and favourable pharmacological properties [46]. We investigated the interplay
417 between *lncMB3*-targeting LNA GapmeRs and standard MB chemotherapeutic approaches,
418 revealing synergistic effects that enhance drug cytotoxicity. This combinatorial approach likely stems
419 from both treatments acting on the intrinsic apoptotic pathway [34] and the TGF-β cascade. These
420 findings suggest that modulating the *lncMB3* molecular network could amplify the efficacy of
421 anticancer agents, paving the way for RNA-based combinatorial strategies to reduce tumour
422 resistance and improve treatment outcomes. However, one of the major challenges in RNA-based
423 therapies is ensuring efficient delivery of effectors to the intended sites. We explored the application
424 of HFt-based nanocarriers for deploying LNA GapmeRs to target *lncMB3*. HFt unique properties, from
425 high biocompatibility and stability to low toxicity and production costs, make it a powerful tool for
426 drug delivery [13]. Moreover, HFt ability to cross the blood-brain barrier [13] positions it as a
427 promising tool for brain tumour-targeting therapies. Finally, ferritin symmetrical self-assembly, small
428 uniform size, and versatile surface functionalisation make it ideal for bioactive compound delivery,
429 including small nucleic acids. Though HFt has been employed to administer siRNAs [49] and

430 microRNAs [50], this work represents, to our knowledge, the first example of gene silencing via HFt-
431 encapsulated ASOs. The combined administration of *lncMB3*-targeting NPs and cisplatin reproduced
432 the synergistic effects observed with ASO transfection, impacting on the TGF-β pathway and
433 reducing cell survival. These results indicate that HFt-based strategies hold promise for targeting
434 oncogenic pathways at the RNA level through biocompatible delivery of tumour-specific antisense
435 oligomers.
436 In conclusion, this study highlights the critical role of *lncMB3* in regulating apoptosis in G3 MB cells
437 through modulation of the TGF-β pathway and interaction with underexplored molecular players
438 such as HMGN5. *LncMB3* stands out as a regulatory node in the G3 MB pathway, linking MYC
439 amplification to increased tumour cell survival by cell death inhibition (Fig. 7). Future efforts will
440 focus on further investigating *lncMB3* interactions and regulatory mechanisms, as well as validating
441 the therapeutic potential of targeting the lncRNA network in preclinical G3 MB models using the HFt
442 nanocarriers.
443
444 **MATERIALS AND METHODS**
445 **Cell Cultures**
446 All cell lines were obtained from ATCC. Semi-adherent D283 Med cells were cultured in MEM
447 medium (M2279, Sigma-Aldrich) supplemented with 20% of heat-inactivated foetal bovine serum
448 (USA origin), 1% Sodium Pyruvate, 1% MEM Non-Essential Amino Acids Solution, 1% Glutamax, and
449 1x Penicillin/Streptomycin. Adherent HD-MB03 cells were cultured in RPMI medium (R0883, Sigma-
450 Aldrich) supplemented with 10% of heat-inactivated foetal bovine serum (USA origin), 1%
451 Penicillin/Streptomycin.
452
453 **Cell Propagation**

454 D283 Med floating cell subpopulation was collected, whereas adherent cell fraction was washed
455 with 1x PBS w/o Ca^{++}/Mg^{++} and detached by incubation in 1x Trypsin/EDTA (T4299, Sigma-Aldrich)
456 for 5 min. Cell fractions were centrifuged at 800 RPM for 5 min and resuspended in fresh culture
457 medium. HD-MB03 cells were washed, detached, centrifuged and resuspended as described above.
458 Cells were counted on a CytoSMART Cell Counter (CLS6749, Corning, Sigma-Aldrich) and replated at
459 the desired concentration.
460
461 **Evaluation of Viable Cell Number**
462 D283 Med cells and HD-MB03 cells were seeded in plates, treated according to experimental plans
463 (GapmeR/plasmid transfection and/or chemotherapeutic treatment) and counted at different time
464 points. Specifically, 10µL cell aliquots were thoroughly suspended, mixed to 10µL of trypan blue dye
465 and counted by CytoSMART Cell Counter for cell population quantifications.
466
467 **Plasmids construction**
468 **Δ16**: D283 Med cell cDNA was used as template to amplify with DNA oligos MB3 FW and MB3 REV
469 (Table 2) a mutant version of *lncMB3* sequence lacking GapmeR #1 terminal binding site. EPB-PURO-
470 TT backbone was linearised with DNA oligos Delta16 FW - T7 REV (Table 2). Construct was generated
471 using In-Fusion Snap Assembly Cloning Kit (Takara Bio).
472 **sh_HMGN5:** was obtained by linearising the EPB-BSD-PGK backbone with DNA oligos
473 shRNA_TOOL_fw and shRNA_TOOL_rev (Table 2). Construct was generated using In-Fusion Snap
474 Assembly Cloning Kit (Takara Bio). Control plasmid was obtained by [25].
475 sh_HMGN5 sequence: GTTGTTGAAGAAGACTACAAT
476
477 **Transfections**

478 LNA GapmeRs: negative control (LG00000002, Qiagen) or specific LNA GapmeRs (Qiagen) were
479 transfected 1-3 times (every 24 hours) in D283 Med or HD-MB03 cells at a concentration of 100 nM
480 with Lipofectamine 2000 (11668-019, Invitrogen, ThermoFisher Scientific), in opti-MEM medium
481 (31985070, Gibco, ThermoFisher Scientific), according to manufacturer's instructions.
482 Control (empty EPB-PURO-TT) and Δ16 plasmids were transfected in D283 Med cells at 100 ng with
483 Lipofectamine 2000 (11668-019, Invitrogen, ThermoFisher Scientific), in opti-MEM medium
484 (31985070, Gibco, ThermoFisher Scientific), according to manufacturer's instructions. Doxycycline
485 100 ng/mL (D9891, Sigma Aldrich, Merck KGaA) was added in the complete growing medium.
486 Five µg of sh_SCR (negative control) or sh_HMGN5 plasmids were transfected twice (24 and 48 hours
487 after cell seeding) in D283 Med cells with Lipofectamine 2000 (11668-019, Invitrogen), in opti-MEM
488 medium (31985070, Gibco, ThermoFisher Scientific), according to manufacturer's instructions.
489
490 **RNA Extraction and Analysis by qRT-PCR**
491 Total RNA was extracted by Direct-zol RNA MiniPrep (R2052, Zymo Research). For quantitative real-
492 time PCR (qRT-PCR) assay, cDNA was synthesised by Takara PrimeScript RT Reagent Kit (RR037A,
493 Takara-bio). qRT-PCR detection was performed using SensiFAST SYBR Lo-ROX Kit (BIO-94020, Bioline)
494 on a 7500 Fast Real-Time PCR (Applied Biosystem). *GAPDH* or *ATP5O* were used as a reference target.
495
496 **Digital PCR analysis**
497 Digital PCR analysis was performed on the QIAcuity® nanoplate digital PCR 8.5K 24-well (Qiagen).
498 The PCR reaction mix was prepared following the manufacturer's instructions. Twelve µl of the final
499 PCR mix were loaded on each nanoplate well, and then automatically sub-aliquoted in 8500
500 partitions. The EVA green signal acquisition was performed with an exposure duration of 500 ms and
501 a gain of 6.

502

503 **Immunoblotting**

504 Protein samples for immunoblotting were extracted from MB cells in RIPA Buffer (50 mM Tris–HCl
505 (pH 8), 150 mM EGTA, 150 mM NaCl, 50 mM NaF, 10% glycerol, 1.5 mM $MgCl_2$, 1% Triton). Lysates
506 were separated on gradient poly-acrylamide gels and transferred to Amersham Protran 0.45 µm
507 nitrocellulose membrane (10600002, GE Healthcare Life Sciences), through the NuPAGE System
508 (EI0002, Invitrogen). Immunoblots were incubated with the following antibodies: anti-GAPDH (sc-
509 32233, Santa Cruz Biotechnology); anti-FLAG (F1804, Sigma-Aldrich); anti-cleaved PARP-1 (bsm-
510 52408R, Bioss); anti-PARP-1 (PA5-34803); anti-HMGN5 (720391, Invitrogen); anti-OTX2 (ab183951,
511 Abcam); anti-BCL2L1 (2764S, Cell Signaling); anti-ATP5O (A305-419A, Bethyl Laboratories). Protein
512 staining was performed by WesternBright ECL (K-12045-D50, Advansta), detected by ChemiDoc XRS+
513 Molecular Imager (Bio-Rad) and quantified through the Image Lab Software (release 3.0.1).

514

515 **RNA-Seq and differential expression analysis**

516 TruSeq Stranded mRNA Library Prep Kit (Illumina, San Diego, CA, USA) was used to obtain sequencing
517 libraries from polyA+ RNA extracted from D283 Med cells (3 independent biological replicates). The
518 sequencing reaction produced 100 nucleotide-long paired-end reads and was performed on a
519 Novaseq 6000 sequencing system (Illumina) with a depth of more than 20M. To remove adapter
520 sequences and low-quality end bases, Trim Galore188 (version 0.6.4_dev) software was used; the
521 minimum read length after trimming was set to 20. Alignment to human GRCh38 genome primary
522 assembly was performed using STAR (version 2.7.9a189). Quality of the sequencing data was
523 assessed with FastQC. More than 85% of the reads were uniquely mapped to the human genome.
524 The "--quantMode TranscriptomeSAM" option was used to generate alignments translated into
525 transcript coordinates. The expression levels of transcripts and genes were quantified by using

526 RSEM. Differential expression analysis (DEA) was performed using the Bioconductor package
527 "DESeq2". Only those genes that showed an absolute expression level of at least 10 in minimum
528 three of the six samples were retained for the DEA. Shrinked logFC values were obtained by the
529 function "lfcShrink". FDR < 0,05 and |logFC| > 0,6 were considered differentially expressed and used
530 for further analysis.
531
532 **Gene Ontology**
533 Gene Ontology (GO) overrepresentation analysis was performed using the DAVID tool
534 (https://david.ncifcrf.gov/tools.jsp) on Wikipathways databases. GO analysis was conducted on both
535 significantly upregulated and downregulated genes.
536
537 **Gene Set Enrichment Analysis**
538 Gene Set Enrichment Analysis (GSEA) was performed by using the Bioconductor package "fgsea".
539 The whole gene set of the experiment was employed and, specifically, logFC and padj values. Using
540 this information, genes were ranked in a sample dataset by multiplying $-\log_{10}$(FDR) * logFC according
541 to their differential expression between two experimental groups. Ensemble Gene IDs were mapped
542 to Entrez Gene IDs using BioMart, and the "fgsea" function was run with minSize = 15, maxSize = 500
543 and nPermSimple = 10000. The analysis was performed on the gene sets belonging to the Molecular
544 Signatures Database (MsigDb v7.4). For each gene set, an enrichment score was computed and
545 assigned to the gene set of the ranked gene lists. Additionally, GSEA calculated a normalised
546 enrichment score to account for variations in pathway size, ensuring robustness across different
547 gene sets and datasets. An FDR of 25% was used for this analysis.
548
549 **Treatments with chemotherapeutics**

550 Chemotherapeutics (cisplatin, HY-17394, MedChem; vincristine HY-N0488, MedChem) were
551 resuspended in DMSO and administered at different concentrations according to the experimental
552 plan. For combined treatments, the selected amount of drug was administered 5 hours after
553 transfections. Cells were counted/analysed 24/48 hours after treatment.
554
555 **Flow Cytometry Analyses**
556 Apoptosis induction was analysed by flow cytometry determination of Annexin V-FITC staining (Enzo
557 Life Sciences, ALX-850-020), to discriminate viable (FITC-/PI-), early apoptotic (FITC+/PI-) and late or
558 necrotic cells (FITC+/PI+). Briefly, cells were collected and resuspended in binding buffer containing
559 Annexin V-FITC and incubated at RT for 15 min. PI was added before reading the sample to flow
560 cytometer (BD FACSCalibur; Beckman Coulter - CytoFLEX SRT). Data were analysed using the Flowing
561 software. Ten thousand events were collected from each sample.
562
563 **Native RNA pull-down assay**
564 Native RNA pulldown experiments were performed as described in [25]. Briefly, 1x10^8 proliferating
565 D283 Med cells were centrifuged at 400 g for 5 min and pellets were lysed for 30 min on rotating
566 wheel at 4°C in Cell Lysis Buffer (Tris-HCl pH 7,5 50 mM, NaCl 150 mM, MgCl2 3 mM, NP40 0,5%,
567 EDTA 2 mM, DTT 1 mM; 1× PIC and RNase inhibitors). The lysate was cleared by centrifugation at
568 15000 g for 15 min at 4°C. One mg of supernatant (whole cell extract) was diluted in a 1:2 ratio with
569 Hybridization Buffer (Tris-HCl pH 7,5 100 mM, NaCl 300 mM, MgCl2 1 mM, SDS 0,2%, Formamide
570 15%, NP40 0,5%, EDTA 10 mM, DTT 1 mM, 1× PIC and RNase inhibitor).
571 10% of the total extract was collected for the Input sample. 100 pmol of biotinylated probes (EVEN,
572 ODD and LacZ sets, see Table probes) were heated at 80°C for 3 minutes and added to the mix. After
573 4-hour incubation on rotating wheel at 4°C, 0,1 ml of washed streptavidin Magnasphere

574 paramagnetic beads (Promega) were added, and the mixture was incubated for as before. After pull-
575 down, beads were collected using a magnetic rack and washed 4 times with Hybridization Buffer.
576 Then 500 µL triZOL (ThermoFisher Scientific) were added to each sample and RNA was extracted
577 (RNeasy Mini Kit Qiagen), DNase-treated and retro transcribed using SuperScript Vilo cDNA
578 Synthesis Kit (ThermoFisher Scientific). Pull-down qRT-PCR results were represented as a percentage
579 of enrichment related to INP.
580
581 **AMT-crosslinked RNA pull-down assay**
582 AMT-crosslinked RNA pull-down experiments were performed as described in [25]. Briefly, 1x10^8
583 D283 Med cells were centrifuged at 400 g for 5 min, resuspended in 10 mL of ice-cold complete PBS
584 supplemented with 0,5 mg/ml 4'-aminomethyl-4,5',8-trimethylpsoralen (AMT, Sigma-Aldrich), and
585 crosslinked at 365 nm five times for 2-minutes cycles. Guanidine Hydrochloride 6M was added 1:1
586 to AMT volume. The lysate was split into 250µL aliquots and 25µL of a 20mg/mL solution of
587 Proteinase K (Ambion) and 6,5µL of 20% SDS were added to each aliquot and incubated at 65°C for
588 1 h. Then 750µL triZOL (ThermoFisher Scientific) were added to each sample and RNA was extracted
589 (RNeasy Mini Kit Qiagen). 50µg of purified AMT-crosslinked RNA were used for each RNA pull-down
590 sample. 500µL of RNAse-free water were added to each sample and heated at 95°C for 2 minutes
591 and then put on ice. 1 volume of 2x Binding Buffer (containing Tris-HCl pH 7,5 20mM, NaCl 1M, EDTA
592 2mM, SDS 0,1%) was added to 1 volume of sample with RNAse inhibitors. 10% of the total extract
593 was collected for the Input sample. 500 pmol of biotinylated probes (EVEN, ODD, LacZ sets, see Table
594 2) were added to the mix and samples were heated at 65°C for 3 minutes. After 4-hour incubation
595 on rotating wheel at 4°C, 0,5ml of washed streptavidin Magnasphere paramagnetic beads (Promega)
596 were added, and the mixture was incubated for 2h at 4°C on rotating wheel. After pull-down, beads
597 were collected using a magnetic rack and washed 4 times with hybridization buffer. Then 500µL

598 triZOL (ThermoFisher) were added to each sample and RNA was extracted (RNeasy Mini Kit Qiagen),
599 UV-decrosslinked at 254nm for 10 minutes, DNase-treated and retro transcribed using SuperScript
600 Vilo cDNA Synthesis Kit (ThermoFisher Scientific). Pull-down (PD) qRT-PCR results were represented
601 as a percentage of enrichment related to INP.
602
603 **Pull down-RNAseq and pre-processing**
604 Raw reads in FASTQ format were retrieved from Illumina BaseSppace and adaptors removed with
605 *fastp* tool. Clean reads were aligned to a GRCh38 assembly using STAR aligner software. Gene *loci*
606 fragment quantification was performed on a customised gene annotation file (GTF file) based on
607 Ensemble (release 87), using the *–quantMode GeneCounts* parameter. The GTF file was previously
608 edited adding the *lncMB3* gene genomic coordinates and annotations. Read counts were combined
609 into a count matrix and processed with DESeq2 R package for normalisation and differential
610 expression analysis. The padj threshold was set to 0,05 to consider DEGs as statistically significant.
611
612 **Pull down-RNAseq analysis**
613 edgeR was used to quantify significant genes as putative interactors on *lncMB3*, using a generalised
614 linear model (GLM) to test for each gene. Statistically significant genes were obtained by separately
615 comparing and intersecting EVEN and ODD samples *vs* Input samples, and then subtracting genes
616 obtained in the comparison between LacZ *vs* Input samples. Only genes with positive FC were used
617 and retained as putative interactors.
618
619 **RNA–RNA interaction prediction**
620 RNA–RNA interaction prediction was computed using IntaRNA 3.3.2 giving as input the full FASTA
621 sequences of transcripts of interest, using the default parameters.

622

623 **microRNA *in silico* predictions**

624 TargetScan Human database, release 8, was exploited to obtain candidates microRNA families
625 targeting genes of interest. MicroRNA families were filtered by choosing those conserved among
626 vertebrates and mammals, then we selected those with conserved sites on the target transcripts,
627 and finally we filtered out the families having more than -0,20 cumulative weighted context++ score,
628 considered as the beginning of moderate confidence level of interaction. Interaction predictions
629 were run by using a locally downloaded version of the interaction prediction tool RNA22.

630

631 **Crosslinking Immunoprecipitation assay**

632 For Crosslinking Immunoprecipitation (CLIP) assay 3,5x10^7 D283 Med cells were grown, UV-
633 crosslinked at 4000×100 µj/cm2 (energy) and collected in NP-40 lysis buffer (50 mM HEPES-KOH,
634 150mM KCl, 2mM EDTA, 1mM NaF, 0,5% (v/v) NP40 pH 7,4, 0,5mM DTT) by low sonication and
635 centrifugation at 20.000 rcf. For immunoprecipitation, 2mg of cytoplasmic extracts were incubated
636 with 10µg of AGO2 antibody or IgG as a control, and coupled to ProteinG Dynabeads resin (10004D,
637 Invitrogen) and 10% was collected as Input. After washing with high-salt buffer (50mM HEPES-KOH,
638 pH7,5, 500mM KCl, 0,05%(v/v) NP40, 0,5mM DTT), immunoprecipitated proteins (20% of the
639 sample) were collected in RIPA buffer and analysed by immunoblotting. Immunoprecipitated RNA
640 (80% of the sample) was treated by Proteinase K, extracted by Direct-zol RNA MiniPrep (Zymo
641 Research), retro-transcribed by Superscript Vilo cDNA synthesis Kit (11754050, Invitrogen) and
642 analysed by qRT-PCR using specific primers. RNA enrichments were reported as percentage of the
643 input.

644

645 **Ribotagging and RNA Immunoprecipitation**

646 1,5x10^7 D283 Med cells were transfected with 15µg of FLAG-RPL22 expressing plasmid. On the day
647 after, cell populations were splitted in two fractions and each sample was treated with 100nM
648 gap_SCR or gap_*lncMB3*, respectively. 24 hours after GapmeRs administration, lysates were
649 prepared in 350µL of POLYSOME LYSIS BUFFER (HEPES 10mM pH 7, KCl 100mM, MgCl2 5mM, NP-40
650 0,5%, dH20) and NT2 BUFFER, Tris 50mM pH 7,5, NaCl 150mM, MgCl2 1mM, NP-40 0,05%, dH2O).
651 150µL of extracts were incubated with 10µg of FLAG antibody (SLBD6976, Sigma Aldrich) or IgG
652 (ultrapure mouse IgG, MU-003-N, Immunoreagents) as control and precipitated through ProteinG-
653 Dynabeads resin (10004D, Invitrogen). 30µL were collected as Input. Immunoprecipitated proteins
654 (20% of the sample) were prepared in loading dye for immunoblot. Immunoprecipitated RNA (80%
655 of the sample) was extracted by Direct-zol RNA MiniPrep (Zymo Research), retro-transcribed by
656 Superscript Vilo cDNA synthesis Kit (11754050, Invitrogen) and analysed by qRT-PCR using specific
657 primers. RNA enrichments were reported as percentage of the input.
658
659 **HFt-HIS-PASE cloning, expression and purification**
660 The design of HFt-HIS-PASE protein, a variant of the HFt-MP-PASE gene previously reported [36],
661 includes, C- to N-terminus: (a) a first domain, comprising the amino acid sequence of the native
662 human ferritin HFt modified through the inclusion of a 5-histidine peptide sequence, inserted in the
663 external loop (referred as CD loop) of the ferritin surface; (b) a second N-terminal domain comprising
664 the amino acid sequence of the matrix metalloproteinase (MMP) cleavage site (PLGLAG) followed
665 by a Proline, Serine, Alanine, and Glutamate (PASE) sequence (ASPAAPAPASPAEPAPSAPA). The
666 expression vector pET-27b containing the HFt-HIS-PASE gene was assembled by GENEART AG
667 (Thermo Fisher Scientific), considering codon optimisation for high expression levels in *E. coli*. BL21
668 (DE3) strain (New England BioLabs).

669 HFt-HIS-PASE was produced with a typical yield of 50mg of pure protein per litre of culture. Cells
670 harbouring the recombinant gene were grown o.n. at 23°C and then at 37°C up to OD600: 1,0, in 1
671 L of terrific broth medium (Grisp), containing 0,03mg/mL kanamycin (Serva). After induction with
672 1mM Isopropil-β-D-tiogalattopiranoside (PanReac) bacteria were incubated at 30°C for 2 hours,
673 harvested by centrifugation at 5000 rpm for 20 minutes at 4°C, resuspended in phosphate-buffered
674 saline (PBS) complemented with 150mM NaCl and 20mM imidazole, pH 7,4, protease inhibitors
675 (ThermoFisher Scientific) and 1mM Phenylmethylsulfonyl fluoride (ThermoFisher Scientific). DNAse
676 (0,1 mg/mL final concentration, Sigma-Aldrich) was added before cell disruption by sonication. The
677 lysate was incubated at 37°C for 40 minutes and centrifuged at 14000 rpm for 50 minutes at 4°C.
678 The supernatant was recovered and loaded in a buffer-equilibrated His-Trap column (Cytiva) for
679 metal affinity chromatography. HFt-HIS-PASE was purified by 100mM imidazole-containing elution
680 buffer, dialysed o.n. against PBS, pH 7,5, and concentrated by 100kDa Amicon Ultra-15 centrifugal
681 filter devices (Millipore). Finally, HFt-HIS-PASE was sterile filtered and stored at 4 °C (short-term) or
682 -20°C (long-term). Preparation purity was assessed by protein staining with Coomassie brilliant blue
683 after a run on 15% SDS-PAGE. Protein concentrations were spectrophotometrically determined at
684 280 nm, using a molar extinction coefficient (on a 24-mer basis) of 4,56×105 M-1cm-1 (ProtParam
685 sofware, http://www.expasy.org).
686
687 **HFt-HIS-PASE characterisation**
688 Size-Exclusion Chromatography experiments were performed using a Superose 6 gel-filtration
689 column equilibrated with PBS at pH 7,4. All samples were prepared at 1mg/mL in filtered ddH2O. All
690 the traces for SEC experiments were analysed with QtiPlot (IONDEV SRL, Bucuresti, Romania).
691
692 **HFt-HIS-PASE fluorescent labelling**

693 The HFt-HIS-PASE protein (1mg/mL) was incubated with 1mM Fluorescein-5-Maleimide (λex 491 nm,
694 λem 518 nm; ThermoFisher Scientific) in PBS, pH 7 for 2 hours at R.T., under stirring in the dark. The
695 sample was filtered, dialysed, and exchanged with PBS as described above. The sample was sterile
696 filtered and stored at 4 °C in the dark. The number of dyes linked per protein was determined by
697 absorbance spectroscopy, in accordance with the manufacturer's instructions, applying the
698 Lambert–Beer law.
699
700 **Synthesis of HFt-HIS-PASE-GapmeR complex**
701 GapmeR #1 was encapsulated within the internal cavity of the HFt-HIS-PASE using reversible, pH-
702 dependent cage dissociation (acid pH) and re-association (neutral pH), in the presence of bioactive
703 payload. HFt-HIS-PASE dissociation into subunits was achieved by lowering pH to 2,8 by 0,1M HCl.
704 GapmeR #1 was added to the disassembled protein solution at a molar ratio of 1:1. The pH was then
705 adjusted to 7,4 by 0,1M NaOH, the solution was ultra-filtered at pH 7,4 and exchanged with PBS by
706 100kDa Amicon Ultra-15 centrifugal filter devices to remove unbound molecules.
707
708 **Characterisation of HFt-HIS-PASE-GapmeR complex**
709 Electrophoresis on 1,8% agarose gel (AGE) of the purified ferritin-GapmeR complexes was used to
710 demonstrate the loading of GapmeRs in the protein cavity. The gel was run at 90V for 60 min stained
711 with Nucleic Acid SYBR Gold for DNA/RNA visualisation and imaged by ChemiDoc™ (Bio-Rad,
712 America). The amount of GapmeR bound to the ferritin NPs was evaluated by the Image J software
713 (https://imagej.net/ij/), by calculating the area and statistics value of pixels in user-defined selection-
714 objects based on intensity. The same analysis was used to evaluate the concentration of the protein
715 using standards of HFt-HIS-PASE as reference after gel staining with Coomassie dye. Purity and
716 hydrodynamic volume of the HFt-HIS-PASE-GapmeR complexes were determined by SEC

717 experiments. To verify GapmeR encapsulation and protection, HFt-HIS-PASE-GapmeR sample was
718 incubated at 37°C for 1 hour and overnight with 12,5x103 U/mL Denarase (c-LEcta GmbH) to digest
719 DNA and RNA impurities. AGE was used as previously described to determine the GapmeR intensity
720 of each sample. AGE was also employed to check the stability of HFt-HIS-PASE-GapmeR NPs stored
721 at 4 °C for 3 months.
722
723 **HFt-HIS-PASE-GapmeR delivery**
724 HFt-HIS-PASE-empty and HFt-HIS-PASE-GapmeR complexes were added to D283 Med cell complete
725 growing medium at a concentration of 200nM and maintained for 48 hours. In HFt/DDP double
726 treatment experiments 5µM DDP was added to cells 2 hours after HFt-HIS-PASE administration.
727
728 **Cytoplasm and nucleus staining**
729 D283 Med cells were cultured as previously described on 0,01% poly-L-ornithine/Murine Laminin
730 20µg/ml (Sigma Aldrich)-coated coverslips, fixed in 4% paraformaldehyde (Electron Microscopy
731 Sciences) for 20 min at 4 °C and washed with PBS. Fixed cells were then permeabilised and blocked
732 with 0,2% Triton X-100/3% BSA/PBS for 15 min at RT. Subsequently, cells were incubated for 45 min
733 at RT in a solution containing 1% donkey and 1% goat serum in PBS, Alexa Fluor™ 555 Phalloidin
734 1:100 (A34055, Invitrogen) to mark actin filaments. After washing with PBS, nuclei were
735 counterstained with DAPI solution (1 µg/ml/PBS, D9542, Sigma Aldrich) and the coverslips were
736 mounted using ProLong Diamond Antifade Mountant (Thermo Fisher Scientific, P-36961).
737
738 **Confocal Microscopy**
739 Samples were imaged using an Olympus iX83 FluoView1200 laser scanning confocal microscope.
740 Acquisitions were performed with a 60X oil objective (NA 1,35) and a 20x objective (NA 0,75) and

741 images were acquired in 16-bit with a resolution of 800 x 800 pixels. For each acquisition with the
742 60X objective, at least 30 focal planes were imaged with a step size of 0,3µm. For each acquisition
743 with the 20X objective, at least 50 focal planes were imaged with a step size of 0,5µm.
744
745 **Cell Count Analysis**
746 Cell counting was performed using an Olympus iX83 FluoView1200 laser scanning confocal
747 microscope with a 20X objective (NA 0,75). Images were acquired in 16-bit with a step size of 0,5µm
748 over at least 50 focal planes. A threshold was set for DAPI (blue, nuclear staining) and for FTH (green,
749 wavelength 488) signals. A maximum intensity projection was created from the Z-stack using Fiji,
750 resulting in a binarised image.
751 The Fiji "Analyse Particles" tool was employed with a minimum size of 25^2 pixels per field. This
752 approach allowed for the counting of particles in each field for both the green and DAPI signals. The
753 number of green cells was calculated relative to the total number of DAPI-marked cells, providing a
754 percentage of green signal delivery.
755
756 **Colocalisation Analysis**
757 Colocalisation between signals was analysed using the "JACoP" Fiji plugin. The green signal
758 (wavelength 488 nm), representing FTH, and the red signal (wavelength 555 nm), provided by
759 Phalloidin for cytoplasmic staining, were assessed for colocalisation. Cell nuclei were identified using
760 DAPI (blue). JACoP thresholds of 290 for the green signal and 181 for the blue (DAPI) or red
761 (Phalloidin) signals were applied to all the acquisitions to evaluate the percentage of colocalisation.
762 Manders' coefficients were used to determine the overlap between the signals, with the
763 colocalisation percentages indicating the extent of the signal overlap.
764

765 **Statistical Analyses**

766 Results are expressed as mean ± SEM from at least 3 biological replicates. In specific cases single
767 experiments were analysed (biological replicates are indicated in figure legends). Statistical
768 differences between groups were analysed by two-tailed Student's *t*-test (performed with GraphPad
769 QuickCalcs). A *p*-value < 0,05 was considered statistically significant. * $p < 0,05$, ** $p < 0,01$, *** $p <$
770 0,001, **** p < 0,0001. One-way analysis of variance (ANOVA) was applied to multi-group data
771 comparisons, followed by Fisher's LSD test.

772

773 **Oligonucleotides and probes**

774 Oligonucleotide, probe and GapmeR sequences are listed in Table 2.

775

776 **MAIN FIGURE LEGENDS**

777 **Figure 1. Differential gene expression analysis upon *lncMB3* KD in G3 MB cells**

778 **A.** Left Panel: heatmap showing the relative levels of DEGs according to RNA-Seq analyses, along
779 with genes hierarchical clustering (3 biological replicates for each condition). The heatmap
780 represents only the DEGs. Right Panel: volcano plot showing DEG distribution. Genes were plotted
781 based on statistical significance $-\log_{10}$(FDR) and differential expression $\log_2$(FC). Downregulated
782 genes (logFC < -0,6) are indicated by the blue dots; upregulated genes (logFC > 0,6) by red dots.
783 Invariant genes are indicated in black.

784 **B**. GO (wikipathways) showing the distribution in clusters of the DEGs in gap_lncMB3 *vs* gap_SCR-
785 treated D283 Med cells, according to RNA-seq data. Categories are listed considering $-\log_{10}$(pvalue)
786 (left panel). qRT-PCR validation analysis of TGF-β pathway genes in D283 Med cells treated for 72
787 hours with gap_SCR or gap_*lncMB3* (GapmeR #1, right panel). Expression levels were compared to
788 gap_SCR sample as control, set as 1. Data (means ± SEM) are expressed in arbitrary units and are

789 relative to *GAPDH* mRNA levels. *N* = 3, * *p* ≤ 0,05, ** *p* ≤ 0,01, *** *p* ≤ 0,001 (two- tailed Student's *t*-

790 test).

791 **C.** qRT-PCR analysis of TGF-β pathway genes in D283 Med cells treated for 72 hours with gap_SCR or

792 gap2_*lncMB3* (GapmeR #2, left panel), or in HD-MB03 cells treated as above (GapmeR #2, right

793 panel). Expression levels were compared to gap_SCR sample as control, set as 1. Data (means ± SEM)

794 are expressed in arbitrary units and are relative to *GAPDH* mRNA levels. *N* = 3 to 5, * *p* ≤ 0,05, ** *p*

795 ≤ 0,01, *** *p* ≤ 0,001 (two- tailed Student's *t*-test).

796

797 **Figure 2. Expression of *OTX2*, *NRL*, *CRX* and *BCL2L1* in MB**

798 **A.** *OTX2*, *NRL*, *CRX* and *BCL2L1* mRNA expression in 4 healthy cerebella (normal samples) and 59

799 primary MB samples according to the transcriptomic dataset GSE164677. Results are expressed in

800 $\log_2$(FPKM). * p ≤ 0,05, ** p ≤ 0,01, *** p ≤ 0,001 **** p ≤ 0,0001 (two-tailed Student's *t*-test).

801 **B.** Schematic representation of *OTX2* network on apoptosis (left panel). GSEA biological process (BP)

802 domains performed on deregulated genes. Categories are listed considering -$\log_{10}$(pvalue) (middle

803 panel). qRT-PCR analysis of *OTX2*, *NRL*, *CRX* and *BCL2L1* in D283 Med cells treated for 72 hours with

804 gap_SCR or gap_*lncMB3* (GapmeR #1, right panel). Expression levels were compared to gap_SCR

805 sample as control, set as 1. Data (means ± SEM) are expressed in arbitrary units and are relative to

806 *GAPDH* mRNA levels. *N* = 3, ** p ≤ 0,01, *** p ≤ 0,001 (two- tailed Student's *t*-test).

807 **C.** Western blot analysis of OTX2 and BCL2L1 protein levels in D283 Med cells treated for 72 hours

808 with gap_SCR or gap_*lncMB3* (GapmeR #1). Normalisations were performed relative to GAPDH

809 protein levels. N = 3, * *p* ≤ 0,05, *** *p* ≤ 0,001, (two-tailed Student's t-test).

810 **D.** Western blot analysis of PARP1 protein levels in D283 Med cells treated for 72 hours with gap_SCR

811 or gap_*lncMB3* (GapmeR #1). Details as in panel C.

812

813 **Figure 3. Analysis of TGF-β pathway and apoptosis in G3 MB cells**

814 **A.** qRT-PCR analysis of *OTX2*, *NRL*, *CRX* and *BCL2L1* in HD-MB03 cells treated for 72 hours with
815 gap_SCR or gap_*lncMB3* (GapmeR #1). Expression levels were compared to gap_SCR sample as
816 control, set as 1. Data (means ± SEM) are expressed in arbitrary units and are relative to *GAPDH*
817 mRNA levels. $N = 3$, * $p \leq 0{,}01$ (two- tailed Student's *t*-test).

818 **B.** Western blot analysis of OTX2 (left panel) and BCL2L1 (right panel) protein levels in HD-MB03 cells
819 treated for 72 hours with gap_SCR or gap_*lncMB3* (GapmeR #1). Normalisations were performed
820 relative to GAPDH protein levels. N = 3, * $p \leq 0{,}05$, *** $p \leq 0{,}001$, (two-tailed Student's t-test).

821 **C.** Time course analysis of the number of viable HD-MB03 cells depleted for *lncMB3* (gap_*lncMB3*).
822 Scramble-transfected cells (gap_SCR) were used as control. Cells were transfected at day 0 (D0) and
823 counted at each timepoint. Data (means ± SEM) are expressed as the number of viable cells, counted
824 by an automated cell counter. $N = 4$, ** $p \leq 0{,}01$, (two-tailed Student's *t*-test).

825 **D.** Western blot analysis of c-PARP1 (left panel) and PARP1 (right panel) protein levels in HD-MB03
826 cells treated for 72 hours with gap_SCR or gap_*lncMB3* (GapmeR #1). $N = 3$, ** $p \leq 0{,}01$, *** $p \leq$
827 $0{,}001$. Details as in panel B.

828 **E.** Dose-response analysis of the number of viable D283 Med cells after TGF-β inhibition. Control
829 cells were treated with vehicle (DMSO). Cell counts started 24 hours after treatment. Data (means ±
830 SEM) are expressed as the number of viable cells, counted by an automated cell counter. $N = 4$, * p
831 $\leq 0{,}05$, ** $p \leq 0{,}01$ (two-tailed Student's *t*-test).

832 **F.** Annexin V staining of D283 Med cells upon TGF-β inhibition. Left panel: representative flow
833 cytometry analysis of propidium iodide- and Annexin V-stained cells. Right panel: quantification of
834 the fractions (expressed as percentage of total cell number) of viable (Annexin V-/PI-), early
835 apoptotic (Annexin V+/PI-), late apoptotic (Annexin V+/PI+) and necrotic (Annexin V-/PI+) cells. For
836 early+late apoptotic cells, $N = 3$, * $p \leq 0{,}05$ (two-way ANOVA). **G.** Left panel: schematic

837 representation of the construct overexpressing *lncMB3* Δ16. Middle panel: qRT-PCR analysis of
838 *lncMB3* expression in D283 Med cells transfected with gap_SCR, gap_*lncMB3* or gap_*lncMB3* + Δ16
839 construct. *N* = 5. Details as in panel A. Right panel: number of viable D283 Med cells upon
840 gap_*lncMB3* transfection (*lncMB3* KD) or Δ16 co-expression, compared to gap_SCR condition.
841 Normalisation was performed on *lncMB3* KD condition. *N* = 5, ** $p \leq 0{,}01$ (two- tailed Student's *t*-
842 test).
843
844 **Figure 4. Analysis of *lncMB3-HMGN5* mRNA interaction**
845 **A.** qRT-PCR analysis of RNA enrichment in EVEN, ODD and LacZ fractions over Input, from native
846 *lncMB3* RNA pull-down experiments of D283 Med cell extracts. Data expressed as percentage of
847 Input, *N* = 2.
848 **B.** Venn diagram showing intersections of mRNAs retrieved and sequenced from two independent
849 native *lncMB3* pull-down fractions (EVEN, ODD, LacZ).
850 **C.** *HMGN5* mRNA expression in 4 healthy cerebella (normal samples) and 59 primary MB samples
851 according to the transcriptomic dataset GSE164677. Results are expressed in $\log_2$(FPKM).
852 * $p \leq 0{,}05$, ** $p \leq 0{,}01$, *** $p \leq 0{,}001$, **** $p \leq 0{,}0001$ (two-tailed Student's *t*-test).
853 **D.** qRT-PCR analysis of *HMGN5* mRNA enrichment in native *lncMB3* RNA pull-down fractions. Details
854 as in panel A.
855 **E.** IntaRNA energy map representing the predicted stability of RNA-RNA interaction between *lncMB3*
856 and *HMGN5* mRNA. mRNA and lncRNA sequences are positioned along the x- and y-axes,
857 respectively. The free energy of predicted intramolecular pairs ranges from red (higher energy,
858 unstable pairing) to blue (minimal energy, stable pairing).

859 **F.** qRT-PCR analysis of *lncMB3* (left panel) and *HMGN5* mRNA (right panel) enrichment in EVEN, ODD
860 and LacZ fractions over Input, from AMT-crosslinked *lncMB3* RNA pull-down experiment in D283
861 Med cells. Data expressed as percentage of Input, *N* = 1.
862 **G.** Western blot analysis of HMGN5 protein levels in D283 Med cells treated for 72 hours with
863 gap_SCR or gap_*lncMB3* (GapmeR #1) or gap_*lncMB3* + Δ16 construct for *lncMB3* recovery.
864 Normalisations were performed relative to GAPDH protein levels. N = 3, * $p \leq 0{,}05$, (two-tailed
865 Student's t-test).
866 **H.** qRT-PCR analysis of *HMGN5* and *GAPDH* upon RPL22-FLAG RIP assay in gap_SCR and gap_*lncMB3*
867 (GapmeR #1) conditions. Analysis of RNA enrichment in IP and IgG fractions over Input. *N* = 1. Data
868 expressed as percentage of Input.
869 **I.** qRT-PCR analysis of *HMGN5*, *INHBE*, *SMAD3*, *OTX2*, *BCL2L1* mRNAs in D283 Med cells treated for
870 72 hours with sh_SCR or sh_HMGN5. Expression levels were compared to sh_SCR sample as control,
871 set as 1. Data (means ± SEM) are expressed in arbitrary units and are relative to *GAPDH* mRNA levels.
872 *N* = 3, * $p \leq 0{,}05$, ** $p \leq 0{,}01$ (two- tailed Student's *t*-test).
873 **J.** Western blot analysis of c-PARP1 (left panel) and PARP1 (right panel) protein levels in D283 Med
874 cells treated for 72 hours with sh_SCR or sh_HMGN5. N = 3, * $p \leq 0{,}05$ (two-tailed Student's t-test).
875 **K.** Analysis of number of viable D283 Med cells treated for 72 hours with sh_SCR or sh_HMGN5.
876 Data (means ± SEM) are expressed as the number of viable cells, counted by an automated cell
877 counter. *N* = 3, * $p \leq 0{,}05$ (two-tailed Student's *t*-test).
878
879 **Figure 5. Analysis of *lncMB3* targeting and DDP treatment on D283 Med cell viability and**
880 **apoptosis**
881 **A.** Left Panel: Dose-response analysis of the number of viable D283 Med cells upon DDP treatment.
882 Control cells (NT) were treated with the DDP vehicle (DMSO). Cell counts were conducted 24 hours

883 after DDP administration. *N* = 1. Middle Panel: percentage of viable D283 Med cells following DDP
884 administration and *lncMB3* GapmeR transfection (GapmeR #1, middle panel; GapmeR #2, right
885 panel). Cell counts were conducted 48 hours after DDP/GapmeR treatments.
886 Double-treated samples (gap_SCR+DDP and gap_*lncMB3*+DDP) were normalised on the viable cell
887 number of the corresponding transfected-only sample (gap_scr and gap_*lncMB3*, respectively). DDP
888 concentration used was 10µM. *N* = 4, * p ≤ 0,05 (two- tailed Student's t-test).
889 **B.** Apoptosis analysis of D283 Med cells following DDP administration [1µM] and GapmeR #1
890 transfection. Left panel: representative flow cytometry analysis of PI- and Annexin V-stained D283
891 Med cells 24 hours after *lncMB3* KD, with or without DPP treatment. Middle panel: quantification of
892 viable (Annexin V-/PI-), early apoptotic (Annexin V+/PI-), late apoptotic (Annexin V+/PI+) and
893 necrotic (Annexin V-/PI+) fractions. *N* = 3, * p ≤ 0,05 (comparison between early + late apoptotic
894 cells). Right panel: percentage of viable D283 Med cells. Data normalisations as in (A). *N* = 3, * p ≤
895 0,05 (two-way ANOVA).
896 **C.** qRT-PCR analysis of TGF-β pathway genes (left panel) and downstream pathway genes (right
897 panel) in D283 Med cells treated for 24 hours with DDP at different doses (reported on the x-axis).
898 Control cells were treated with vehicle (DMSO) and set as 1. Data (means ± SEM) are expressed in
899 arbitrary units and are relative to *GAPDH* mRNA levels. *N* = 3, * *p* ≤ 0,05, ** *p* ≤ 0,01, *** *p* ≤ 0,001
900 (two- tailed Student's *t*-test).
901
902 **Figure 6. Synthesis, analysis and application of HFt-HIS-PASE/GapmeR complexes**
903 **A.** Left panel: representative image of colocalisation analysis between fluorescein-HFt-HIS-PASE and
904 DAPI in D283 Med cells, 12 hours after administration (magnification 20x). Fluorescein-HFt-HIS PASE
905 (green) and DAPI (blue, nuclear staining) are on the left, object counts after binarisation are in the
906 middle and the merge of the two channels is on the right. Right panel: percentage of colocalisation

907 between fluorescein-HFt-HIS-PASE and DAPI in D283 Med cells. Data (mean ± SEM) were obtained
908 from 8 different fields.
909 **B.** Left panel: representative immunofluorescence of fluorescein-HFt-HIS PASE delivered for 24 hours
910 (green), DAPI (blue, nuclear staining) and phalloidin (red, cytoplasmic staining) (magnification 60x).
911 Right panel: percentage of nucleus/cytoplasm subcellular localisation of HFt-HIS PASE in D283 Med
912 cells. Data (mean + SEM) were obtained from 5 different fields.
913 **C.** Band migration profiles on agarose gel electrophoresis. Gel was double stained with SYBR Gold
914 for GapmeR visualisation (left panel) and Coomassie Blue for ferritin visualisation (right panel). *Lane*
915 *1*: GapmeR standard 2µM; *Lane 3*: GapmeR standard 1µM; *Lane 5*: GapmeR standard 0,5µM; *Lane*
916 *6*: HFt-HIS-PASE-GapmeR complex.
917 **D.** Size Exclusion Chromatography profile analysis of HFt-HIS-PASE (in black), HFt-HIS-PASE-GapmeR
918 #1 complexes (in red) and GapmeR #1 alone (in blue).
919 **E.** qRT-PCR analysis of *lncMB3* levels in D283 Med cells upon treatment with HFt-HIS-PASE-GapmeR
920 #1 complexes, 48 hours after delivery, compared with empty HFt-HIS-PASE, set as 1. Data (means ±
921 SEM) are expressed in arbitrary units and are relative to *GAPDH* mRNA levels. $N = 3$, *** $p \leq 0{,}001$
922 (two- tailed Student's *t*-test).
923 **F.** qRT-PCR analysis of TGF-β pathway genes in D283 Med cells treated for 48 hours with HFt-HIS-
924 PASE-GapmeR #1 + 5µM DDP. Expression levels were compared to HFt-HIS-PASE-empty + 5µM DDP,
925 set as 1. Data (means ± SEM) are expressed in arbitrary units and are relative to *GAPDH* mRNA levels.
926 $N = 3$, * $p \leq 0{,}05$, ** $p \leq 0{,}01$ (two- tailed Student's *t*-test).
927 **G.** Analysis of number of viable D283 Med cells treated for 48 hours with HFt-HIS-PASE-GapmeR #1
928 + 5µM DDP. HFt-HIS-PASE empty + 5µM DDP was used as control condition. Data (means ± SEM) are
929 expressed as the percentage of viable cells, counted by an automated cell counter. $N = 4$, ** $p \leq 0{,}01$
930 (two-tailed Student's *t*-test).

931

932 **Figure 7.** Schematic representation of the MYC-dependent *lncMB3* mechanism of action. Image

933 made with Biorender (https://biorender.com).

934

935 **SUPPLEMENTARY FIGURE LEGENDS**

936 **Figure S1. *LncMB3* expression – Referred to Figure 1 and 2**

937 **A.** qRT-PCR analysis of *MYC, lncMB3 and OTX2* in a pool of 10 healthy cerebella (cereb) set as 1, in

938 D283 Med cells or in HD-MB03 cells. Data (means ± SEM) are expressed in arbitrary units and are

939 relative to *GAPDH* mRNA levels. $N = 3$, * $p \leq 0{,}05$, ** $p \leq 0{,}01$ (two- tailed Student's *t*-test).

940 **B.** Expression of *lncMB3* from 54 non-diseased tissues, according to Genotype-Tissue Expression

941 (GTEx) Analysis, Release V8. Levels are shown in Transcripts per Million (TPM). Circles represent

942 outliers. Details at https://gtexportal.org/home/gene/RP11-95I16.6.

943

944 **Figure S2. *LncMB3*-dependent transcriptomic analysis in G3 MB cells – Referred to Figure 1**

945 **A.** qRT-PCR analysis of *lncMB3* in gap_SCR samples *vs* gap_*lncMB3* (GapmeR #1) samples. *LncMB3*

946 expression levels upon KD was compared to gap_SCR condition, set as 1. Data (means ± SEM) are

947 expressed in arbitrary units and are relative to *GAPDH* mRNA levels. $N = 3$, *** $p \leq 0{,}001$ (two- tailed

948 Student's *t*-test).

949 **B.** Left panel: the plot reports, for each sequenced sample, the number of detected genes obtained

950 from RNA-Seq analysis. Right Panels: Euclidean distance heatmap showing the similarity in gene

951 expression within the SCR and KD (GapmeR #1) samples. Pearson correlation heatmap showing the

952 similarity in gene expression within the SCR and KD (GapmeR #1) samples.

953 **C.** qRT-PCR analysis of RNA-Seq deregulated transcripts with padj spanning from 0,001 to 0,05 in

954 gap_SCR *vs* gap_*lncMB3* (GapmeR #1) samples. Expression levels upon KD were compared to

955 gap_SCR condition, set as 1. Data (means ± SEM) are expressed in arbitrary units and are relative to
956 *GAPDH* mRNA levels. $N = 3$, * $p \leq 0{,}05$, ** $p \leq 0{,}01$, *** $p \leq 0{,}001$ (two- tailed Student's *t*-test).
957 **D.** Schematic representation of DEG quantitative selection.
958
959 **Figure S3. RNA-Seq data mining – Referred to Figure 1**
960 **A.** qRT-PCR validation of RNA-Seq data in *lncMB3* KD compared to gap_SCR condition, set as 1.
961 Validated candidates (10 RNAs) are indicated in histograms. Data (means ± SEM) are expressed in
962 arbitrary units and are relative to *GAPDH* mRNA levels. $N = 3$, * $p \leq 0{,}05$, ** $p \leq 0{,}01$, *** $p \leq 0{,}001$
963 (two- tailed Student's *t*-test).
964 **B.** GO showing the distribution in clusters of the DEGs in gap_lncMB3 *vs* gap_SCR-treated D283 Med
965 cells, according to RNA-Seq data: Downregulated (BLUE) and Upregulated (RED) sets referring to
966 WikiPathways Database. Categories are listed considering $-\log_{10}$(pvalue).
967 **C**. GSEA showing the differentially expressed TGF-β pathway components in gap_lncMB3 *vs*
968 gap_SCR-treated D283 Med cells, according to RNA-seq data.
969 **D.** Schematic representation of the relevant validated genes in the tumour (G3 MB, left panel) and
970 in the lncMB3 KD condition (right panel). Orange squares highlight the TGF-β pathway components.
971
972 **Figure S4. Validation of *lncMB3* KD specificity – Referred to Figure 1, 2 and 3**
973 **A.** Schematic representation of GapmeR #1 and GapmeR #2 (blue lines) binding to *lncMB3* (black
974 line).
975 **B.** Left histograms: qRT-PCR analysis of *lncMB3* in D283 Med and HD-MB03 cells upon *lncMB3* KD
976 (GapmeR #1). Right histograms: qRT-PCR analysis of *lncMB3* D283 Med and HD-MB03 cells upon
977 *lncMB3* KD (GapmeR #2). $N = 3$, * $p \leq 0{,}05$, ** $p \leq 0{,}01$, *** $p \leq 0{,}001$ (two- tailed Student's).
978

979 **Figure S5. AGO2 CLIP assay in D283 Med cells – Referred to Figure 4**

980 **A.** Left Panel: Western blot analysis of AGO2 levels in AGO2- (IP), IgG-immunoprecipitated cell
981 extracts, and in Input sample, as control. Right panel: qRT-PCR analysis of RNA enrichment over Input
982 in IP and IgG fractions. *N* = 1. Data expressed as percentage of Input. *GAPDH* and *PTBP1* mRNAs were
983 used as negative and positive control, respectively.

984

985 **Figure S6. Analysis of *lncMB3* mechanism of action – Referred to Figure 4**

986 **A.** Table showing the genes enriched according to the RNA-Seq analysis of two independent native
987 *lncMB3* pull-down assays performed on total extracts of D283 Med cells.

988 **B.** Expression of *HMGN5* from 54 healthy tissues, according to GTEx Analysis, Release V8. Levels are
989 shown in RPKM. Circles represent outliers. Details at https://gtexportal.org/home/gene/HMGN5

990 **C.** Table showing the absolute number of molecules per µL for *lncMB3*, *HMGN5* and *GAPDH*,
991 according to the evaluation performed through digital PCR analysis.

992

993 **Figure S7. Analysis of *lncMB3* mechanism of action – Referred to Figure 4**

994 **A.** qRT-PCR analysis of *HMGN5* mRNA in D283 Med cells upon *lncMB3* KD (GapmeR #1). Data (means
995 ± SEM) are expressed in arbitrary units and are relative to *GAPDH* mRNA levels. *N* = 3, (two- tailed
996 Student's *t*-test).

997 **B.** Western blot analysis of RPL22 protein levels in mock-treated or overexpressing FLAG-RPL22
998 construct D283 Med cells. Normalisations were performed relative to GAPDH protein levels. *N* = 1.

999 **C.** Western blot analysis of RPL22 protein levels in fractions (Inp, IP, IgG) from RIP assay performed
1000 in gap_SCR, or gap_*lncMB3* conditions. Normalisations were performed relative to GAPDH protein
1001 levels. *N* = 1.

1002 **D.** qRT-PCR analysis of pre-mRNAs of the TGF-β and following pathways upon *lncMB3* KD (GapmeR
1003 #1) relative to gap_SCR, set as 1. Data (means ± SEM) are expressed in arbitrary units and are relative
1004 to *GAPDH* mRNA levels. *N* = 3, * $p \leq 0{,}05$, ** $p \leq 0{,}01$, *** $p \leq 0{,}001$ (two- tailed Student's *t*-test).
1005 **E.** Western blot analysis of HMGN5 protein levels in D283 Med cells treated with sh_SCR or
1006 sh_HMGN5 after 72 hours. Normalisations were performed relative to GAPDH protein levels. *N* = 3,
1007 * $p \leq 0{,}05$ (two- tailed Student's *t*-test).
1008 **F.** Table showing the % of downregulation of *INHBE, SMAD3, OTX2 and BCL2L1* upon gap_lncMB3 or
1009 sh_HMGN5 in D283 Med cells.
1010
1011 **Figure S8. Analysis of *lncMB3* targeting and chemotherapeutic treatments on D283 Med cells –**
1012 **Referred to Figure 5**
1013
1014 **A.** qRT-PCR analysis of *lncMB3* in D283 Med cells treated for 24 hours with DDP at different doses
1015 (reported on the x-axis). Control cells were treated with vehicle (DMSO) and set as 1. Data (means ±
1016 SEM) are expressed in arbitrary units and are relative to *GAPDH* mRNA levels. *N* = 3, (two- tailed
1017 Student's *t*-test).
1018 **B.** Right panel: dose-response analysis of the number of viable D283 Med cells upon vincristine
1019 treatment. Cells were treated with the vincristine vehicle (DMSO), 5, 20 or 50µg/mL vincristine,
1020 without GapmeRs or with gap_SCR or gap_*lncMB3* (GapmeR #1). Cell counts were conducted 48
1021 hours after vincristine/GapmeR treatments. *N* = 3, * $p \leq 0{,}05$, ** $p \leq 0{,}01$ (two- tailed Student's). Left
1022 panel: double-treated samples (gap_SCR+vincristine and gap_*lncMB3*+vincristine) were normalised
1023 on the viable cell number of the corresponding transfected-only sample (gap_scr and gap_*lncMB3*,
1024 respectively). Vincristine concentration was 20µg/mL. *N* = 3, (two- tailed Student's t-test).

1025 **C.** Left panel: quantification of c-PARP protein levels in D283 Med cells upon vincristine treatment in
1026 untreated (NT), gap_SCR or gap_*lncMB3* samples, in the same conditions as in panel B. GAPDH was
1027 used as control. Right panel: western blot analysis of c-PARP protein levels from the experiment
1028 described in left panel. Normalisation was performed on GAPDH protein levels. *N* = 1 for each
1029 condition (drug concentration).
1030
1031 **Figure S9 – Molecular analysis related to Hft-HIS-PASE-GapmeR complex delivery – Referred to**
1032 **Figure 6**
1033 **A.** Schematic representation of Hft-HIS-PASE and Hft-HIS-PASE-GapmeR encapsulation in the protein
1034 cavity. Single domains and molecules are described in the legend. To allow the internal surface of
1035 the protein to be visualised (lighter colours), only 18 monomers out of the 24 are shown. In addition,
1036 for clarity purposes, only 4 out of the 24 histidine tags are shown. The picture has been generated
1037 with Pymol and GNU Image Manipulation Programs.
1038 **B.** qRT-PCR analysis of *CD71*, *MMP 2* and *MMP 9* mRNA levels in D283 Med (left panel) or HD-MB03
1039 (right panel) cells. Data (means ± SEM) are expressed in arbitrary units and are relative to *GAPDH*
1040 mRNA levels.
1041 **C.** HFt-HIS-PASE-GapmeR complexes before and after Denarase treatment at 37°C visualised as band
1042 migration profiles on agarose gel electrophoresis. *Lane 1:* HFt-HIS-PASE-GapmeR complex; *Lane 2:*
1043 HFt-HIS-PASE-GapmeR complexes after overnight incubation with Denarase; *Lane 3*: HFt-HIS-PASE-
1044 GapmeR complexes after 1-hour incubation with Denarase. Gel was stained with SYBR Gold.
1045 **D.** qRT-PCR analysis of *lncMB3* levels upon KD with GapmeR #1 (gap_*lncMB3*) or Hft-HIS-PASE-
1046 GapmeR complexes (HFt-gap_*lncMB3*), relative to gap_SCR, set as 1. Data are expressed in arbitrary
1047 units and are relative to *GAPDH* mRNA levels. *N* = 1.
1048

ACKNOWLEDGEMENTS

We acknowledge M. Marchioni and J. Genovese for their experimental assistance, C. Grelloni and A. Giuliani for their technical and analytical suggestions and E. Caffarelli for valuable discussions and laboratory support. FRP was supported by an AIRC fellowship. Confocal microscopy acquisitions were conducted at the Imaging Facility of CLN²S@Sapienza, Istituto Italiano di Tecnologia, Rome. Cytofluorimeters were available at IBPM-CNR. RNA-Seq were performed by DNA Link (Seoul, KR) and by Eclipse Bioinnovation (San Diego, CA).

In memory of M. Arceci, beloved friend and colleague.

FUNDING

This work was supported by grants: from MUR (PRIN 2017, id. 2017P352Z4) to PL; from the European Union - Next Generation EU, within the MUR National Recovery and Resilience Plan (NRRP) - M4C2 - Action 1.4 - Call "Potenziamento strutture di ricerca e di campioni nazionali di R&S", Project CN3 "National Center for Gene Therapy and Drugs based on RNA Technology", no. CN00000041 (Spoke #6 "RNA Drug Development", CUP B83C22002860006 to PL, and Spoke 3 "Neurodegeneration", CUP B83C22002870006 to IB and MB); from the European Union - Next-Generation EU within the MUR National Recovery and Resilience Plan [NRRP] - M4C2 - Action 1.1, Call "PRIN 2022" (id. 2022BYB33L, CUP: B53D23016090006 to MB and PL, and id. 2022WC7BL2, CUP B53D23016520006 to EF); from the European Union - Next GenerationEU within the MUR National Recovery and Resilience Plan [NRRP] - M4C2, Action. 1.1, Call "PRIN 2022 PNRR" – id. P2022FFEWN RNA2FUN, CUP B53D23026140001 to MB; from the National Research Council of Italy (projects DBA.AD005.225-NUTRAGE-FOE2021 and DSB.AD006.371-InvAt-FOE2022) to PL; from Sapienza University (RM12117A5DE7A45B and RM123188F6B80CE4) to MB; from AIRC (IG 2020 N° 24942) to DT and AIRC (IG 2019 Id.23053) to IB and ERC-2019-SyG (855923-ASTRA) to IB.

1073

1074 **AUTHOR CONTRIBUTIONS**

1075 CRedIT author statement. Conceptualisation: AG, PL; Investigation: AG (gene expression analysis,
1076 cloning, molecular and cellular assays), PT (interaction assays, imaging and microscopy), FRP (flow
1077 cytometry), EF and GT (nanovector synthesis and characterisation), AB (gene expression analysis),
1078 AP, FM and AC (bioinformatic analysis); Formal Analysis: AG, PT, FRP, AP, FM, AB and AC; Validation:
1079 AG, PT, FRP, EF, AB and GT; Methodology: AG, PT, FRP, EF, JR and GT; Data Curation: AG, PT, AP, FM
1080 and AC; Software; AP, FM and AC; Visualisation: AG and JR; Resources: AC, IB, DT, MB and EF;
1081 Supervision: AC, DT, MB, PC and PL; Writing – original draft (main text): AG, MB and PL; Funding
1082 Acquisition and Project administration: PL.

1083

1084 **DATA AVAILABILITY**

1085 The RNA-Seq data presented in this study are available in GEO, accession numbers GSE277976 and
1086 GSE278666.

1087

1088 **COMPETING INTERESTS**

1089 The authors declare no competing interests.

1090

1091 **INFORMED CONSENT**

1092 Manuscript is approved by all authors for publication.

1093

1094 **REFERENCES**

1095 [1] P. A. Northcott *et al.*, “Medulloblastoma,” *Nat Rev Dis Primers*, vol. 5, no. 1, p. 11, Feb. 2019,
1096 doi: 10.1038/s41572-019-0063-6.

[2] Q. T. Ostrom *et al.*, “CBTRUS Statistical Report: Primary Brain and Other Central Nervous System Tumors Diagnosed in the United States in 2012–2016,” *Neuro Oncol*, vol. 21, no. Supplement_5, pp. v1–v100, Nov. 2019, doi: 10.1093/neuonc/noz150.

[3] M. C. Vladoiu *et al.*, “Childhood cerebellar tumours mirror conserved fetal transcriptional programs,” *Nature*, vol. 572, no. 7767, pp. 67–73, Aug. 2019, doi: 10.1038/s41586-019-1158-7.

[4] F. M. G. Cavalli *et al.*, “Intertumoral Heterogeneity within Medulloblastoma Subgroups,” *Cancer Cell*, vol. 31, no. 6, pp. 737-754.e6, Jun. 2017, doi: 10.1016/j.ccell.2017.05.005.

[5] M. F. Roussel and J. L. Stripay, “Epigenetic Drivers in Pediatric Medulloblastoma,” *The Cerebellum*, vol. 17, no. 1, pp. 28–36, Feb. 2018, doi: 10.1007/s12311-017-0899-9.

[6] M. F. Roussel and G. W. Robinson, “Role of MYC in Medulloblastoma,” *Cold Spring Harb Perspect Med*, vol. 3, no. 11, pp. a014308–a014308, Nov. 2013, doi: 10.1101/cshperspect.a014308.

[7] J. S. Mattick *et al.*, “Long non-coding RNAs: definitions, functions, challenges and recommendations,” *Nat Rev Mol Cell Biol*, vol. 24, no. 6, pp. 430–447, Jun. 2023, doi: 10.1038/s41580-022-00566-8.

[8] O. Beylerli, I. Gareev, A. Sufianov, T. Ilyasova, and Y. Guang, “Long noncoding RNAs as promising biomarkers in cancer,” *Noncoding RNA Res*, vol. 7, no. 2, pp. 66–70, Jun. 2022, doi: 10.1016/j.ncrna.2022.02.004.

[9] P. Laneve and E. Caffarelli, “The Non-coding Side of Medulloblastoma,” *Front Cell Dev Biol*, vol. 8, May 2020, doi: 10.3389/fcell.2020.00275.

[10] J. Rea *et al.*, “Identification and Functional Characterization of Novel MYC-Regulated Long Noncoding RNAs in Group 3 Medulloblastoma,” *Cancers (Basel)*, vol. 13, no. 15, p. 3853, Jul. 2021, doi: 10.3390/cancers13153853.

[11] M. Morabito *et al.*, “An autocrine ActivinB mechanism drives <scp>TGF</scp> β/Activin signaling in Group 3 medulloblastoma,” *EMBO Mol Med*, vol. 11, no. 8, Aug. 2019, doi: 10.15252/emmm.201809830.

[12] D. C. Adamson *et al.*, “OTX2 Is Critical for the Maintenance and Progression of Shh-Independent Medulloblastomas,” *Cancer Res*, vol. 70, no. 1, pp. 181–191, Jan. 2010, doi: 10.1158/0008-5472.CAN-09-2331.

[13] F. Marrocco *et al.*, “Nose-to-brain selective drug delivery to glioma via ferritin-based nanovectors reduces tumor growth and improves survival rate,” *Cell Death Dis*, vol. 15, no. 4, p. 262, Apr. 2024, doi: 10.1038/s41419-024-06653-2.

[14] J. Kurreck, “Design of antisense oligonucleotides stabilized by locked nucleic acids,” *Nucleic Acids Res*, vol. 30, no. 9, pp. 1911–1918, May 2002, doi: 10.1093/nar/30.9.1911.

1132 [15] A. Weiss and L. Attisano, “The TGFbeta Superfamily Signaling Pathway,” *WIREs*
1133 *Developmental Biology*, vol. 2, no. 1, pp. 47–63, Jan. 2013, doi: 10.1002/wdev.86.

1134 [16] Y. He *et al.*, “Targeting PI3K/Akt signal transduction for cancer therapy,” *Signal Transduct*
1135 *Target Ther*, vol. 6, no. 1, p. 425, Dec. 2021, doi: 10.1038/s41392-021-00828-5.

1136 [17] A. B. Baba *et al.*, “Transforming Growth Factor-Beta (TGF-β) Signaling in Cancer-A Betrayal
1137 Within,” *Front Pharmacol*, vol. 13, Feb. 2022, doi: 10.3389/fphar.2022.791272.

1138 [18] D. Vanhoutte *et al.*, “Thbs1 regulates skeletal muscle mass in a TGFβ-Smad2/3-ATF4-
1139 dependent manner,” *Cell Rep*, vol. 43, no. 5, p. 114149, May 2024, doi:
1140 10.1016/j.celrep.2024.114149.

1141 [19] B. Schmierer and C. S. Hill, “TGFβ–SMAD signal transduction: molecular specificity and
1142 functional flexibility,” *Nat Rev Mol Cell Biol*, vol. 8, no. 12, pp. 970–982, Dec. 2007, doi:
1143 10.1038/nrm2297.

1144 [20] D. Onichtchouk *et al.*, “Silencing of TGF-β signalling by the pseudoreceptor BAMBI,” *Nature*,
1145 vol. 401, no. 6752, pp. 480–485, Sep. 1999, doi: 10.1038/46794.

1146 [21] C.-R. Chen, Y. Kang, P. M. Siegel, and J. Massagué, “E2F4/5 and p107 as Smad Cofactors
1147 Linking the TGFβ Receptor to c-myc Repression,” *Cell*, vol. 110, no. 1, pp. 19–32, Jul. 2002,
1148 doi: 10.1016/S0092-8674(02)00801-2.

1149 [22] A. Nishida *et al.*, “Otx2 homeobox gene controls retinal photoreceptor cell fate and pineal
1150 gland development,” *Nat Neurosci*, vol. 6, no. 12, pp. 1255–1263, Dec. 2003, doi:
1151 10.1038/nn1155.

1152 [23] A. Garancher *et al.*, “NRL and CRX Define Photoreceptor Identity and Reveal Subgroup-
1153 Specific Dependencies in Medulloblastoma,” *Cancer Cell*, vol. 33, no. 3, pp. 435-449.e6, Mar.
1154 2018, doi: 10.1016/j.ccell.2018.02.006.

1155 [24] C. Soldani and A. I. Scovassi, “Poly(ADP-ribose) polymerase-1 cleavage during apoptosis: An
1156 update,” *APOPTOSIS*, vol. 7, no. 4, pp. 321–328, 2002, doi: 10.1023/A:1016119328968.

1157 [25] P. Tollis *et al.*, “The long noncoding RNA nHOTAIRM1 is necessary for differentiation and
1158 activity of iPSC-derived spinal motor neurons,” *Cell Death & Disease 2023 14:11*, vol. 14, no.
1159 11, pp. 1–14, Nov. 2023, doi: 10.1038/s41419-023-06196-y.

1160 [26] P. Laneve *et al.*, “The long noncoding RNA linc-NeD125 controls the expression of
1161 medulloblastoma driver genes by microRNA sponge activity,” *Oncotarget*, vol. 8, no. 19, pp.
1162 31003–31015, May 2017, doi: 10.18632/oncotarget.16049.

1163 [27] C. Grelloni *et al.*, “BRCA1 levels and DNA-damage response are controlled by the
1164 competitive binding of circHIPK3 or FMRP to the BRCA1 mRNA,” *Mol Cell*, Oct. 2024, doi:
1165 10.1016/j.molcel.2024.09.016.

[28] M. Rochman, C. Malicet, and M. Bustin, “HMGN5/NSBP1: A new member of the HMGN protein family that affects chromatin structure and function,” *Biochimica et Biophysica Acta (BBA) - Gene Regulatory Mechanisms*, vol. 1799, no. 1–2, pp. 86–92, Jan. 2010, doi: 10.1016/j.bbagrm.2009.09.012.

[29] C. Malicet, M. Rochman, Y. Postnikov, and M. Bustin, “Distinct Properties of Human HMGN5 Reveal a Rapidly Evolving but Functionally Conserved Nucleosome Binding Protein,” *Mol Cell Biol*, vol. 31, no. 13, pp. 2742–2755, Jul. 2011, doi: 10.1128/MCB.05216-11.

[30] Y. Gan *et al.*, “Knockdown of HMGN5 increases the chemosensitivity of human urothelial bladder cancer cells to cisplatin by targeting PI3K/Akt signaling,” *Oncol Lett*, Sep. 2017, doi: 10.3892/ol.2017.7045.

[31] J. Mou *et al.*, “HMGN5 Escorts Oncogenic STAT3 Signaling by Regulating the Chromatin Landscape in Breast Cancer Tumorigenesis,” *Molecular Cancer Research*, vol. 20, no. 12, pp. 1724–1738, Dec. 2022, doi: 10.1158/1541-7786.MCR-22-0241.

[32] E. Sanz, J. C. Bean, D. P. Carey, A. Quintana, and G. S. McKnight, “RiboTag: Ribosomal Tagging Strategy to Analyze Cell-Type-Specific mRNA Expression In Vivo,” *Curr Protoc Neurosci*, vol. 88, no. 1, Jun. 2019, doi: 10.1002/cpns.77.

[33] J. Enríquez Pérez, S. Fritzell, J. Kopecky, E. Visse, A. Darabi, and P. Siesjö, “The effect of locally delivered cisplatin is dependent on an intact immune function in an experimental glioma model,” *Sci Rep*, vol. 9, no. 1, p. 5632, Apr. 2019, doi: 10.1038/s41598-019-42001-7.

[34] S. Ghosh, “Cisplatin: The first metal based anticancer drug,” *Bioorg Chem*, vol. 88, p. 102925, Jul. 2019, doi: 10.1016/j.bioorg.2019.102925.

[35] C. Seidel, S. Heider, P. Hau, A. Glasow, S. Dietzsch, and R.-D. Kortmann, “Radiotherapy in Medulloblastoma—Evolution of Treatment, Current Concepts and Future Perspectives,” *Cancers (Basel)*, vol. 13, no. 23, p. 5945, Nov. 2021, doi: 10.3390/cancers13235945.

[36] E. Falvo *et al.*, “The presence of glutamate residues on the PAS sequence of the stimuli-sensitive nano-ferritin improves in vivo biodistribution and mitoxantrone encapsulation homogeneity,” *Journal of Controlled Release*, vol. 275, pp. 177–185, Apr. 2018, doi: 10.1016/j.jconrel.2018.02.025.

[37] J. He, S. Xu, and A. J. Mixson, “The Multifaceted Histidine-Based Carriers for Nucleic Acid Delivery: Advances and Challenges,” *Pharmaceutics*, vol. 12, no. 8, p. 774, Aug. 2020, doi: 10.3390/pharmaceutics12080774.

[38] D. N. Louis *et al.*, “The 2007 WHO Classification of Tumours of the Central Nervous System,” *Acta Neuropathol*, vol. 114, no. 2, pp. 97–109, Aug. 2007, doi: 10.1007/s00401-007-0243-4.

[39] E. M. Thompson *et al.*, “Prognostic value of medulloblastoma extent of resection after accounting for molecular subgroup: a retrospective integrated clinical and molecular

analysis," *Lancet Oncol*, vol. 17, no. 4, pp. 484–495, Apr. 2016, doi: 10.1016/S1470-2045(15)00581-1.

[40] K. Juraschka and M. D. Taylor, "Medulloblastoma in the age of molecular subgroups: a review," *J Neurosurg Pediatr*, vol. 24, no. 4, pp. 353–363, Oct. 2019, doi: 10.3171/2019.5.PEDS18381.

[41] O. Menyhárt, F. Giangaspero, and B. Győrffy, "Molecular markers and potential therapeutic targets in non-WNT/non-SHH (group 3 and group 4) medulloblastomas," *J Hematol Oncol*, vol. 12, no. 1, p. 29, Dec. 2019, doi: 10.1186/s13045-019-0712-y.

[42] Y. Dong, R. Tu, H. Liu, and G. Qing, "Regulation of cancer cell metabolism: oncogenic MYC in the driver's seat," *Signal Transduct Target Ther*, vol. 5, no. 1, p. 124, Jul. 2020, doi: 10.1038/s41392-020-00235-2.

[43] V. Llombart and M. R. Mansour, "Therapeutic targeting of 'undruggable' MYC," *EBioMedicine*, vol. 75, p. 103756, Jan. 2022, doi: 10.1016/j.ebiom.2021.103756.

[44] E. Garralda *et al.*, "MYC targeting by OMO-103 in solid tumors: a phase 1 trial," *Nat Med*, vol. 30, no. 3, pp. 762–771, Mar. 2024, doi: 10.1038/s41591-024-02805-1.

[45] A. Dent *et al.*, "HAVOC: Small-scale histomic mapping of cancer biodiversity across large tissue distances using deep neural networks," *Sci Adv*, vol. 9, no. 39, Sep. 2023, doi: 10.1126/sciadv.adg1894.

[46] M. Coan, S. Haefliger, S. Ounzain, and R. Johnson, "Targeting and engineering long non-coding RNAs for cancer therapy," *Nat Rev Genet*, Feb. 2024, doi: 10.1038/s41576-024-00693-2.

[47] V. Ferrucci *et al.*, "Metastatic group 3 medulloblastoma is driven by PRUNE1 targeting NME1–TGF-β–OTX2–SNAIL via PTEN inhibition," *Brain*, vol. 141, no. 5, pp. 1300–1319, May 2018, doi: 10.1093/brain/awy039.

[48] "HMGN5, an RNA or Nucleosome binding protein - potentially switching between the substrates to regulate gene expression", doi: 10.1101/2022.07.15.500188.

[49] L. Li *et al.*, "Ferritin-mediated siRNA delivery and gene silencing in human tumor and primary cells," *Biomaterials*, vol. 98, pp. 143–151, Aug. 2016, doi: 10.1016/j.biomaterials.2016.05.006.

[50] F. R. Liberati *et al.*, "Combined Delivery of miR-15/16 through Humanized Ferritin Nanocages for the Treatment of Chronic Lymphocytic Leukemia," *Pharmaceutics*, vol. 16, no. 3, p. 402, Mar. 2024, doi: 10.3390/pharmaceutics16030402.

FIGURE 1

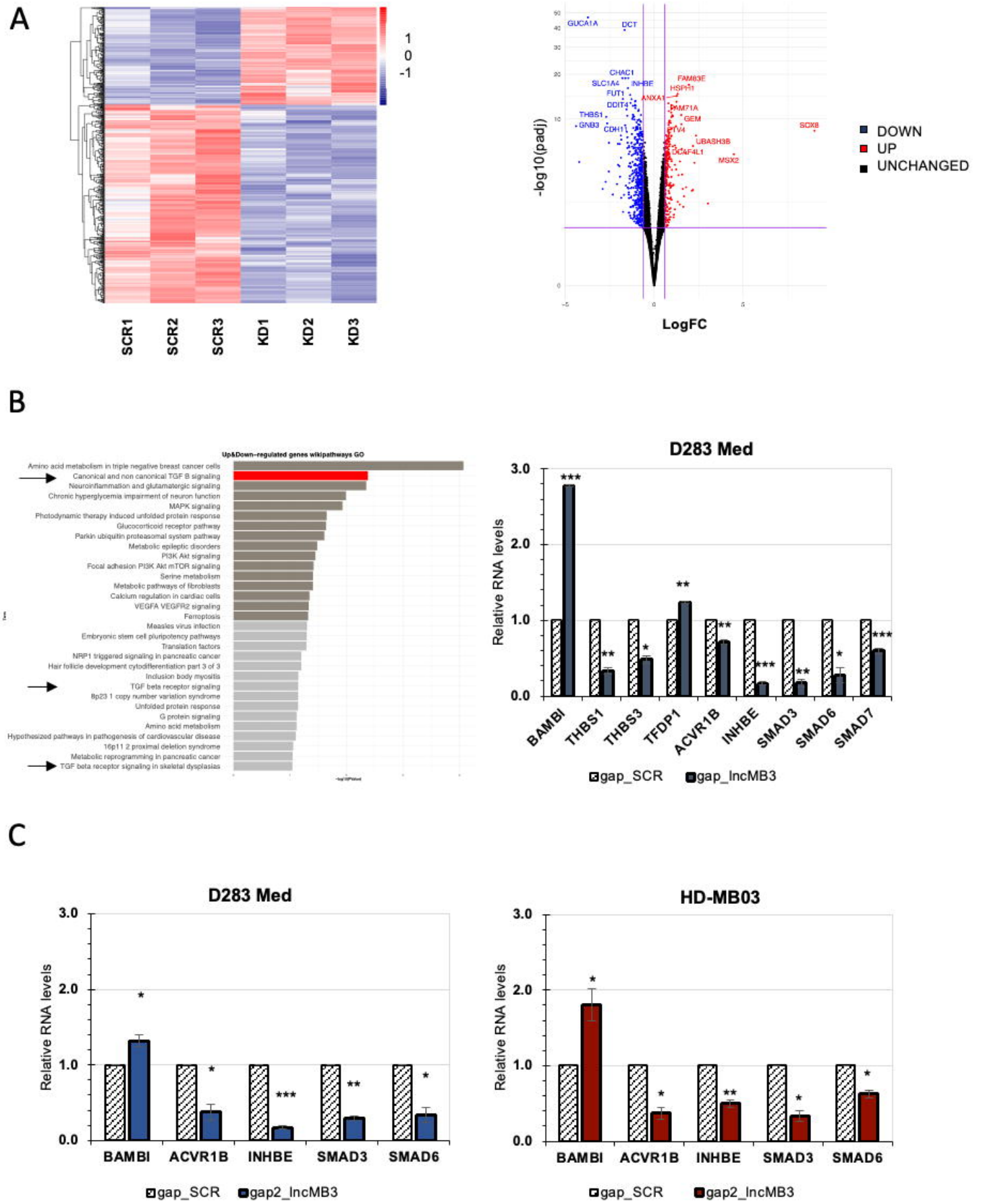
A
1
0
-1
SCR1
SCR2
SCR3
KD1
KD2
KD3
GUCA1A
DCT
CHAC1
SLC1A4
INHBE
FUT1
DDIT4
THBS1
GNB3
CDH1
FAM83E
HSPH1
ANXA1
FAM71A
GEM
PTV4
UBASH3B
DCAF4L1
MSX2
SCX8
-log10(padj)
LogFC
DOWN
UP
UNCHANGED
B
Up&Down-regulated genes wikipathways GO
Amino acid metabolism in triple negative breast cancer cells
Canonical and non canonical TGF B signaling
Neuroinflammation and glutamatergic signaling
Chronic hyperglycemia impairment of neuron function
MAPK signaling
Photodynamic therapy induced unfolded protein response
Glucocorticoid receptor pathway
Parkin ubiquitin proteasomal system pathway
Metabolic epileptic disorders
PI3K Akt signaling
Focal adhesion PI3K Akt mTOR signaling
Serine metabolism
Metabolic pathways of fibroblasts
Calcium regulation in cardiac cells
VEGFA VEGFR2 signaling
Ferroptosis
Measles virus infection
Embryonic stem cell pluripotency pathways
Translation factors
NRP1 triggered signaling in pancreatic cancer
Hair follicle development cytodifferentiation part 3 of 3
Inclusion body myositis
TGF beta receptor signaling
8p23 1 copy number variation syndrome
Unfolded protein response
G protein signaling
Amino acid metabolism
Hypothesized pathways in pathogenesis of cardiovascular disease
16p11 2 proximal deletion syndrome
Metabolic reprogramming in pancreatic cancer
TGF beta receptor signaling in skeletal dysplasias
D283 Med
Relative RNA levels
BAMBI
THBS1
THBS3
TFDP1
ACVR1B
INHBE
SMAD3
SMAD6
SMAD7
gap_SCR
gap_lncMB3
C
D283 Med
Relative RNA levels
BAMBI
ACVR1B
INHBE
SMAD3
SMAD6
gap_SCR
gap2_lncMB3
HD-MB03
Relative RNA levels
BAMBI
ACVR1B
INHBE
SMAD3
SMAD6
gap_SCR
gap2_lncMB3

FIGURE 2

A

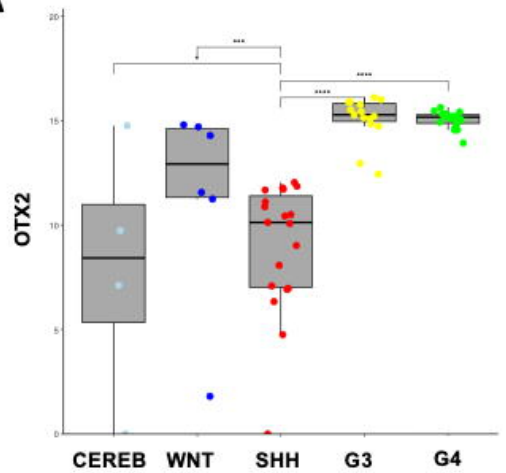

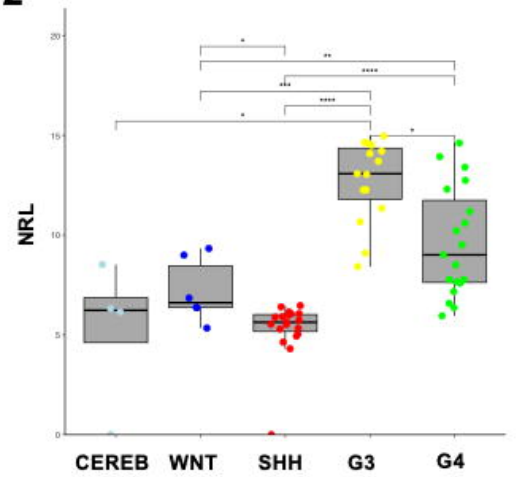

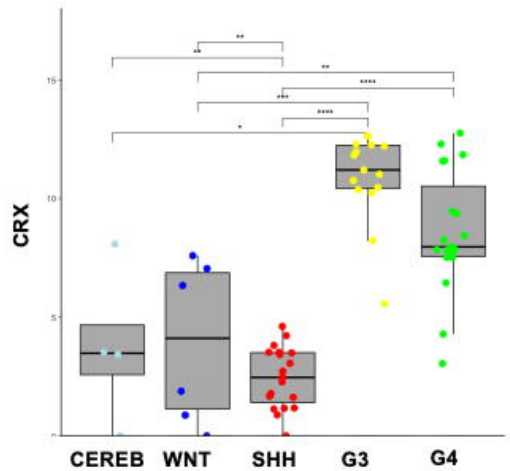

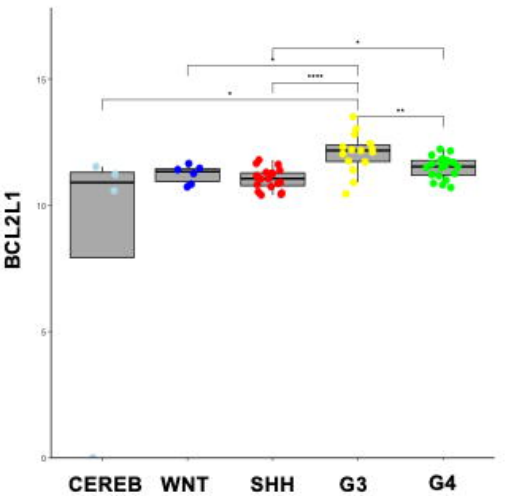

B

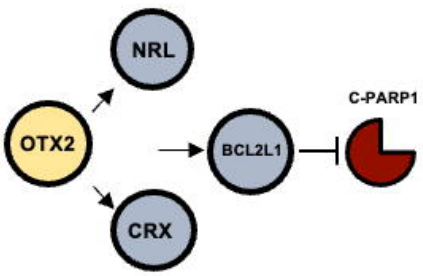

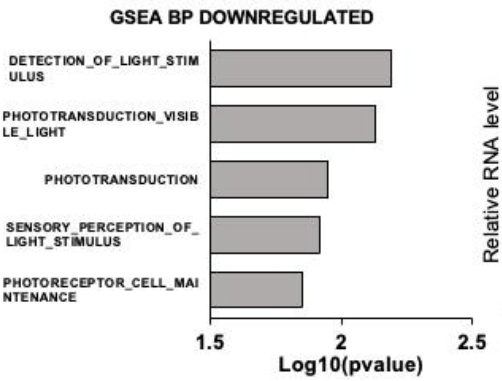

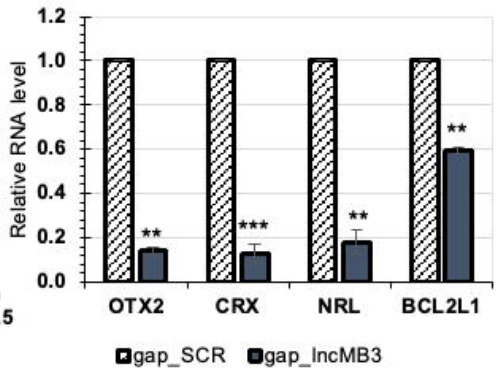

C

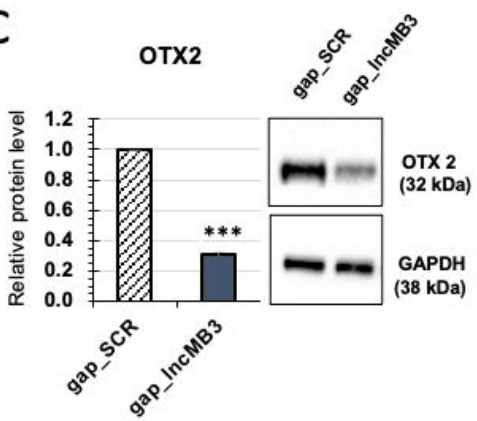

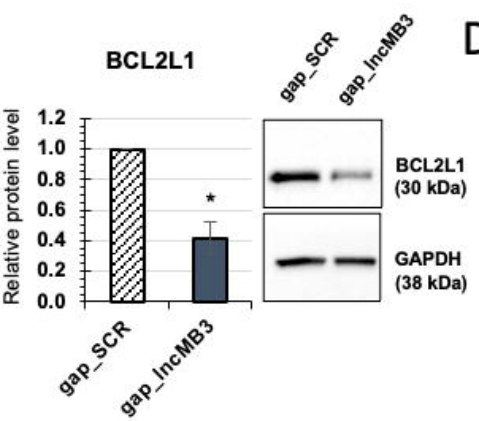

D

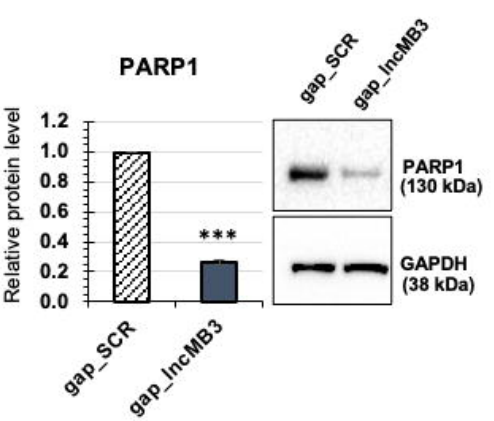

FIGURE 3

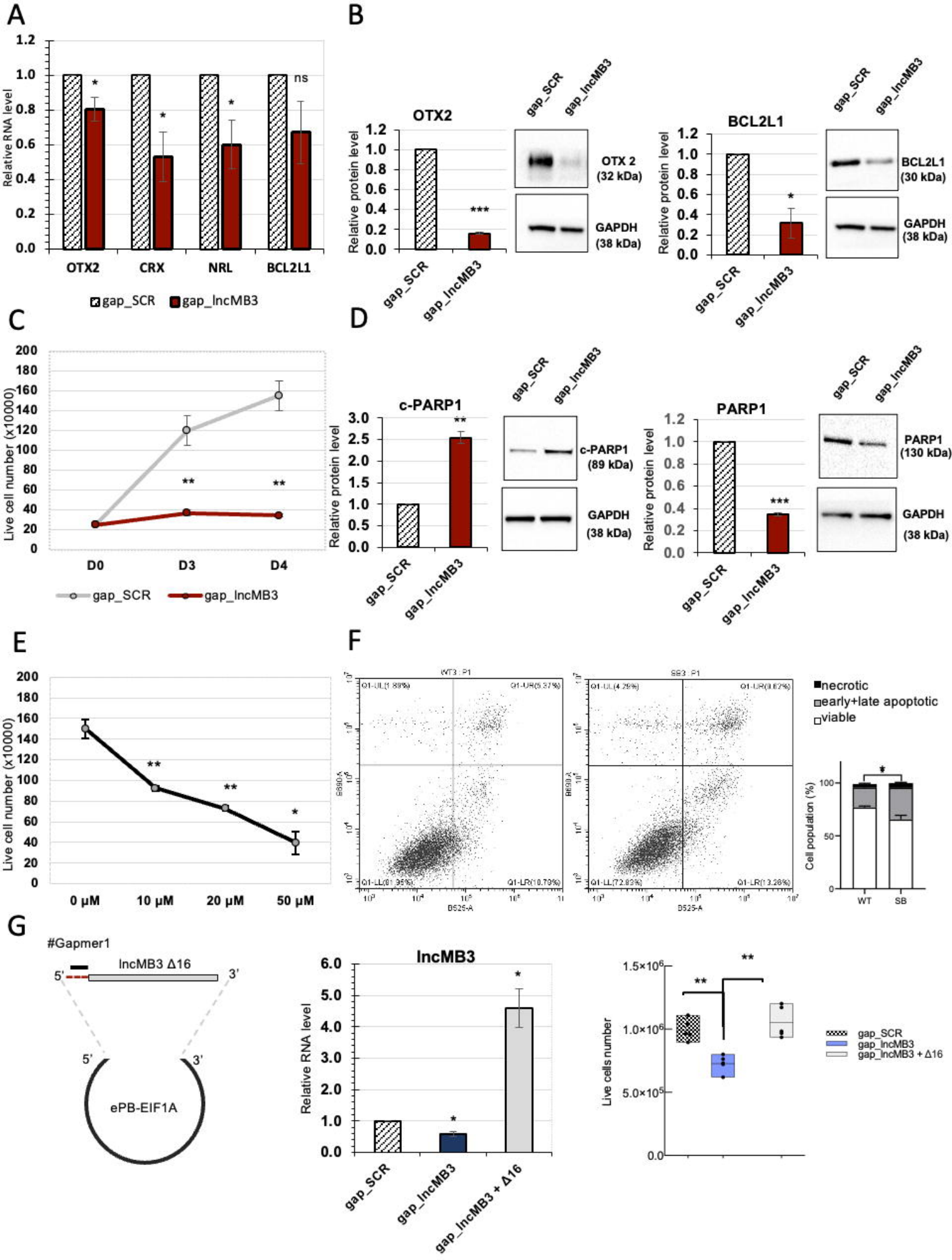
A
Relative RNA level
OTX2
CRX
NRL
BCL2L1
ns
gap_SCR
gap_lncMB3
B
OTX2
Relative protein level
gap_SCR
gap_lncMB3
OTX 2 (32 kDa)
GAPDH (38 kDa)
BCL2L1
BCL2L1 (30 kDa)
C
Live cell number (x10000)
D0
D3
D4
D
c-PARP1
c-PARP1 (89 kDa)
PARP1
PARP1 (130 kDa)
E
0 µM
10 µM
20 µM
50 µM
F
WT3 : P1
SB3 : P1
necrotic
early+late apoptotic
viable
Cell population (%)
WT
SB
G
#Gapmer1
lncMB3 Δ16
5'
3'
ePB-EIF1A
lncMB3
gap_lncMB3 + Δ16
Live cells number
gap_lncMB3 + Δ16

FIGURE 4

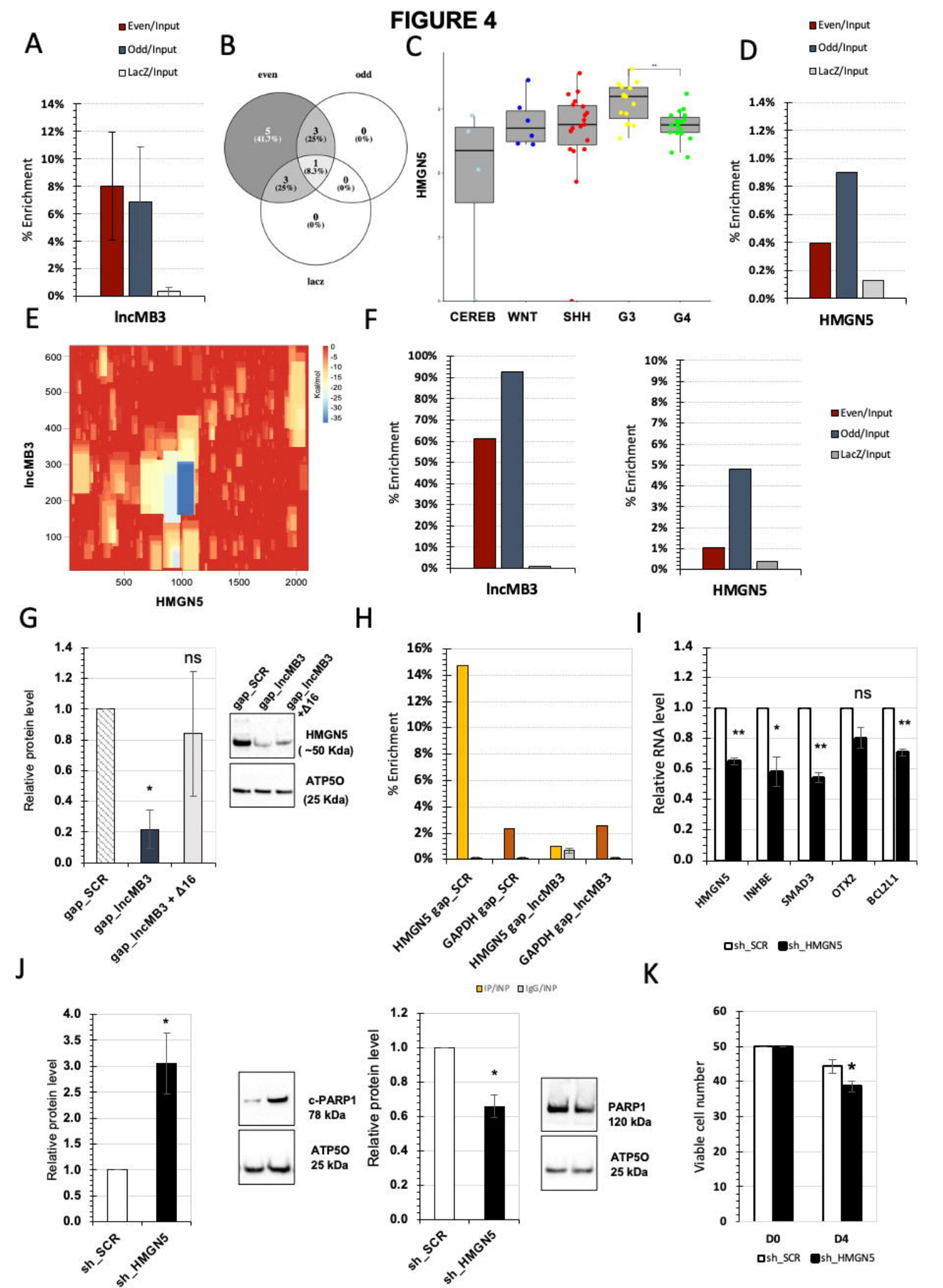
A
Even/Input
Odd/Input
LacZ/Input
% Enrichment
lncMB3
B
even
odd
lacz
5 (41.7%)
3 (25%)
0 (0%)
1 (8.3%)
3 (25%)
0 (0%)
0 (0%)
C
HMGN5
CEREB
WNT
SHH
G3
G4
D
Even/Input
Odd/Input
LacZ/Input
% Enrichment
HMGN5
E
lncMB3
HMGN5
Kcal/mol
F
% Enrichment
lncMB3
HMGN5
Even/Input
Odd/Input
LacZ/Input
G
Relative protein level
ns
gap_SCR
gap_lncMB3
gap_lncMB3 + Δ16
HMGN5 (~50 Kda)
ATP5O (25 Kda)
H
% Enrichment
HMGN5 gap_SCR
GAPDH gap_SCR
HMGN5 gap_lncMB3
GAPDH gap_lncMB3
IP/INP
IgG/INP
I
Relative RNA level
ns
HMGN5
INHBE
SMAD3
OTX2
BCL2L1
sh_SCR
sh_HMGN5
J
Relative protein level
sh_SCR
sh_HMGN5
c-PARP1 78 kDa
ATP5O 25 kDa
Relative protein level
PARP1 120 kDa
ATP5O 25 kDa
K
Viable cell number
D0
D4
sh_SCR
sh_HMGN5

FIGURE 5

A

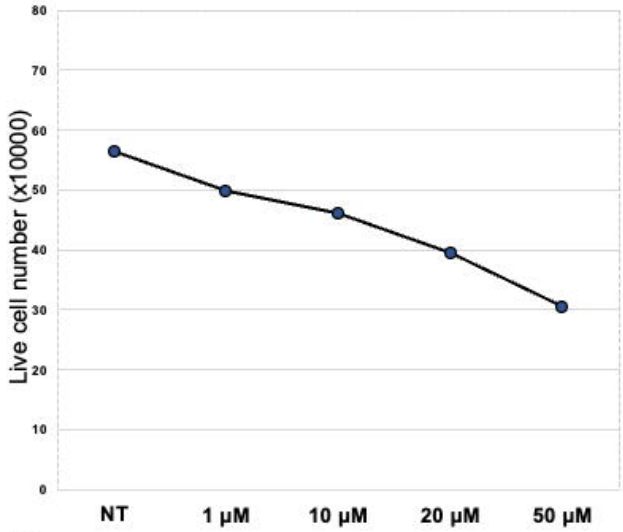
Live cell number (x10000)
80
70
60
50
40
30
20
10
0
NT
1 µM
10 µM
20 µM
50 µM

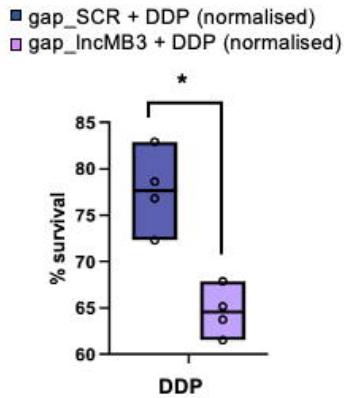
gap_SCR + DDP (normalised)
gap_lncMB3 + DDP (normalised)
*
% survival
85
80
75
70
65
60
DDP

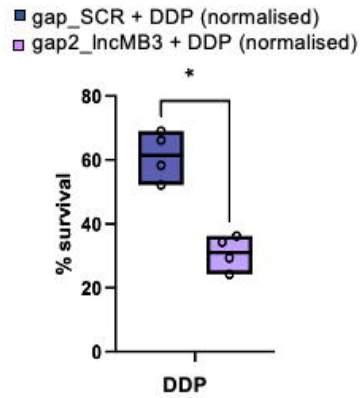
gap_SCR + DDP (normalised)
gap2_lncMB3 + DDP (normalised)
*
% survival
80
60
40
20
0
DDP

B

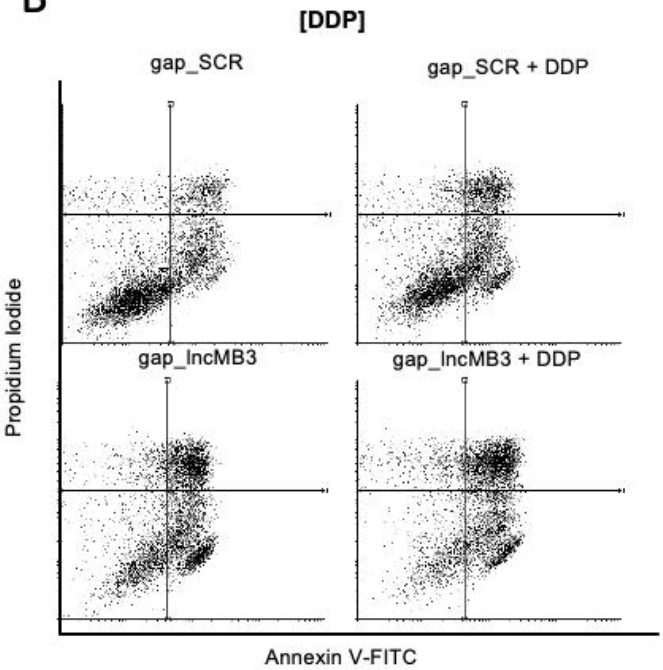
[DDP]
gap_SCR
gap_SCR + DDP
gap_lncMB3
gap_lncMB3 + DDP
Propidium Iodide
Annexin V-FITC

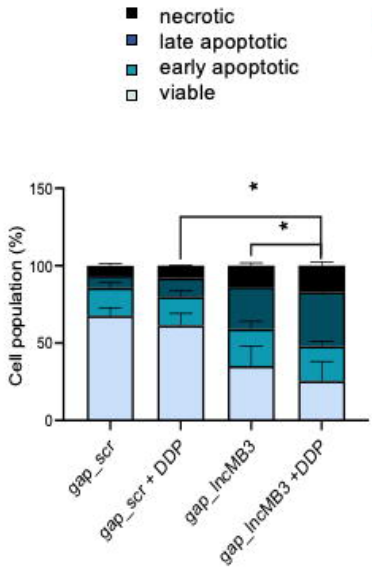
necrotic
late apoptotic
early apoptotic
viable
Cell population (%)
150
100
50
0
*
*
gap_scr
gap_scr + DDP
gap_lncMB3
gap_lncMB3 +DDP

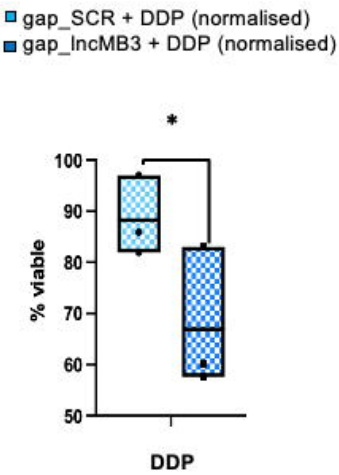
gap_SCR + DDP (normalised)
gap_lncMB3 + DDP (normalised)
*
% viable
100
90
80
70
60
50
DDP

C

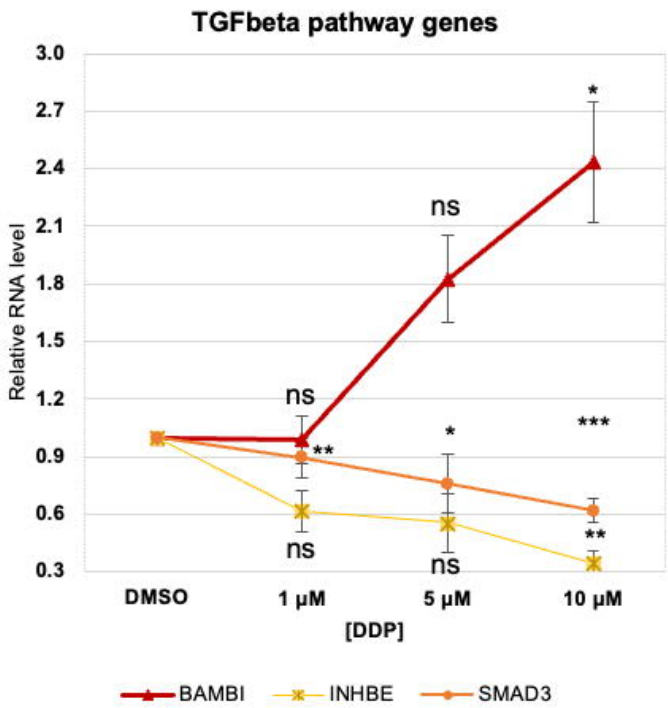
TGFbeta pathway genes
Relative RNA level
3.0
2.7
2.4
2.1
1.8
1.5
1.2
0.9
0.6
0.3
ns
ns
ns
ns
*
**
*
**
***
DMSO
1 µM
5 µM
10 µM
[DDP]
BAMBI
INHBE
SMAD3

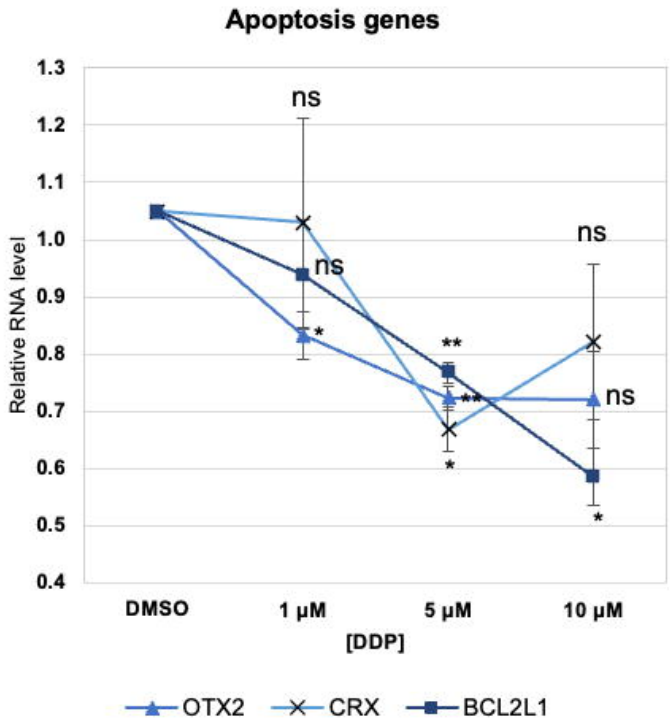
Apoptosis genes
Relative RNA level
1.3
1.2
1.1
1.0
0.9
0.8
0.7
0.6
0.5
0.4
ns
ns
ns
ns
*
**
**
*
*
DMSO
1 µM
5 µM
10 µM
[DDP]
OTX2
CRX
BCL2L1

FIGURE 6

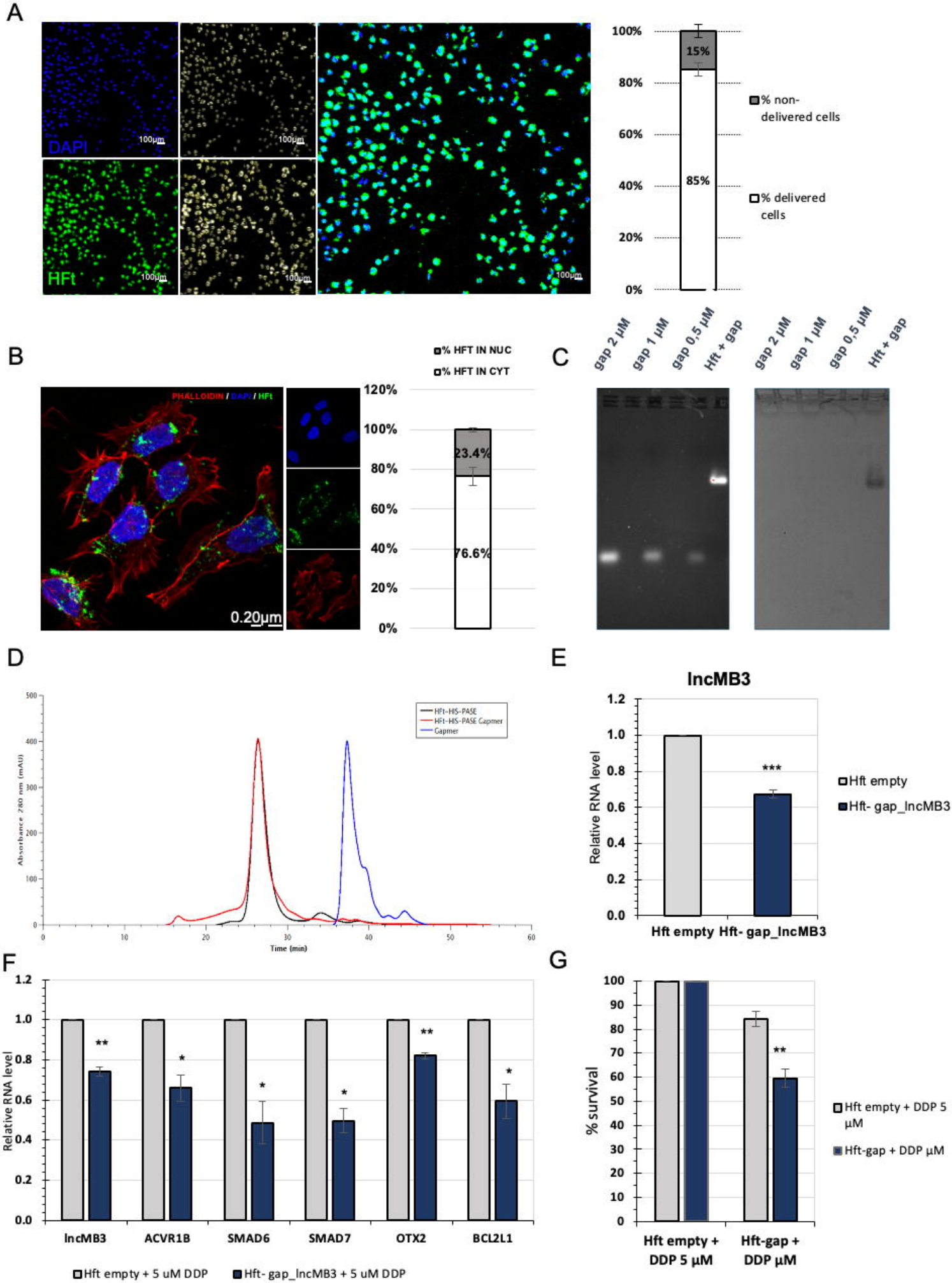
A
DAPI
HFt
100µm
100%
80%
60%
40%
20%
0%
15%
85%
% non-delivered cells
% delivered cells
B
PHALLOIDIN / DAPI / HFt
0.20µm
% HFT IN NUC
% HFT IN CYT
23.4%
76.6%
C
gap 2 µM
gap 1 µM
gap 0,5 µM
Hft + gap
D
Hft-HIS-PASE
Hft-HIS-PASE Gapmer
Gapmer
Absorbance 280 nm (mAU)
Time (min)
E
lncMB3
Relative RNA level
***
Hft empty
Hft- gap_lncMB3
F
Relative RNA level
lncMB3
ACVR1B
SMAD6
SMAD7
OTX2
BCL2L1
Hft empty + 5 uM DDP
Hft- gap_lncMB3 + 5 uM DDP
G
% survival
Hft empty + DDP 5 µM
Hft-gap + DDP µM

FIGURE 7

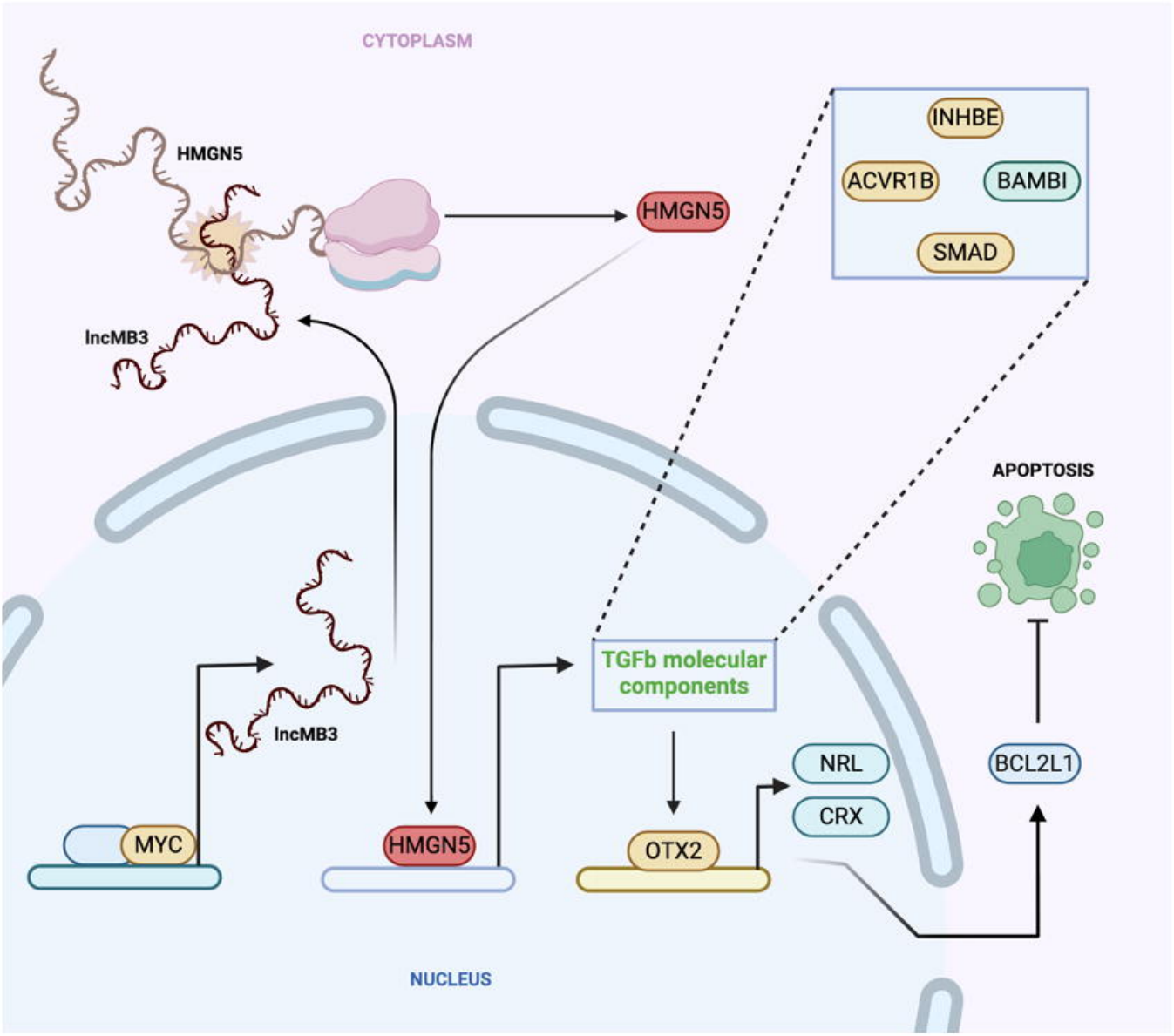
CYTOPLASM
HMGN5
lncMB3
HMGN5
INHBE
ACVR1B
BAMBI
SMAD
APOPTOSIS
TGFb molecular components
lncMB3
NRL
CRX
BCL2L1
MYC
HMGN5
OTX2
NUCLEUS